Jakob Tvedt Jensen

Added ship resistance from headboxes and transverse tunnels in full scale CFD

Master's thesis in Marine Technology
Supervisor: Håvard Holm
June 2020

NTNU
Norwegian University of
Science and Technology

Jakob Tvedt Jensen

Added ship resistance from headboxes and transverse tunnels in full scale CFD

Master's thesis in Marine Technology
Supervisor: Håvard Holm
June 2020

Norwegian University of Science and Technology
Faculty of Engineering
Department of Marine Technology

NTNU

Norwegian University of
Science and Technology

Abstract

A full scale offshore supply vessel with two bow tunnels and headboxes is simulated in calm water to estimate the added resistance from these hull modifications. Holtrop's formula for bow thrusters with drag coefficients $C_{D_{TH}}$ of respectively 0.005 and 0.009 is shown to approximate the added resistance from the foremost and aftmost tunnel well. Least squares fitting with ITTC's recommended formula for appendix resistance gives a form factor k of 2.9 for the headboxes, but the expected Reynolds number dependence of their resistance can not be shown. By consideration of all findings, there is a clear argument that model scale simulations may instead be used for the prediction of tunnel and headbox resistance.

Simulations apply the Reynolds-averaged Navier-Stokes equations. They are closed with the k-ω SST turbulence model. The free surface is resolved with a Volume of Fluid approach, and an equilibrium model is applied for ship motions. Near wall velocities are approximated by wall functions.

While total resistance generally shows good grid convergence, convergence is not clear for all investigated values. When compared to the Grid-convergence index method, a least squares fitting approach gives more appropriately conservative estimates for the discretization uncertainty. For five considered velocities, the mean numerical uncertainty of resistance is estimated to seven percent.

Samandrag

Eit fullskala forsyningsskip med to baugtunnelar og headboksar er simulert i stille vatn for å estimera tilleggsmotstanden frå desse modifikasjonane. Holtrop sin formel for baugtunnelar med koeffisientar $C_{D_{TH}}$ lik 0.005 og 0.009 for fremre og bakre tunnel svarar godt til målt motstand. Likninga ITTC føreslår for appendiksmotstand passar headboksmålingane best med ein formfaktor k lik 2.9, men den venta samanhengen med Reynoldstalet kan ikkje påvisast. Summen av gjorde funn tyder at ein like godt kan simulera i modellskala for å spå motstanden frå tunnelar og headboksar.

Simuleringane løyser Reynoldsmidla Navier-Stokes-likningar (RANSE). Likningane er lukka med turbulensmodellen k-ω SST. Fri overflate er modellert med vekta volumdelar (VOF). Skipsrørsler er funne med ein modell som nyttar låst jamvekt. Logaritmisk grensesjiktstilnærming er brukt for å finna væskefarten nær skrogoverflata.

Totalmotstand viser jamt god gridkonvergens, men konvergens er ikkje tydeleg for alle undersøkte verdiar. Samanlikna med Gridkonvergensindeksmetoda (GCI), gjer kurvetilpassing med minste kvadrat meir konservative og truverdige estimat for den numeriske utryggleika. For fem vurderte snøggleikar er snittet av numerisk utryggleik for totalmotstand sju prosent.

Contents

Acknowledgements

1 Introduction

To find the added resistance of transverse bow tunnels and headboxes, full scale CFD simulations of a vessel with and without these modifications are conducted. Parameters for analytical expressions for added resistance are suggested based on the results. A similar study has been conducted by Christensen[9], who looked at added resistance from bow tunnels in model scale CFD.

The quality of the approach is determined by consideration of modeling simplifications in the CFD methodology, and thorough investigations of grid convergence in both model and full scale. Grid convergence studies are conducted by application of both the Grid-convergence index (GCI), and a least squares based method. Model scale simulations are validated against towing tank results. Validation data is not available for full scale simulations, so results are compared to scaled model test values. The added resistance of the bow tunnels is compared to estimates by Stuntz[4], and Hollenbach[5]. For the headboxes, no direct comparisons have been found.

To reach goals for reduced global greenhouse gas emissions, transport emissions must be decoupled from economic growth[37]. One part of the solution is to lower energy intensity by improving vessel performance. For ships, demands for improved energy intensity are imposed by the International Maritime Organization through Marpol and the Energy efficiency design index (EEDI). These emission regulations are key drivers for advances in ship performance[11]. A prerequisite for improving performance is the ability to accurately predict it.

Predicting the hydrodynamic performance of a vessel is paramount in all phases of design.

While only the performance difference between designs is needed for optimization purposes, accurate predictions of absolute performance are necessary for the determination of project feasibility and for contractual purposes. Calm water resistance is a central aspect of vessel performance. The inclusion of appendices, transverse tunnels or headboxes is determined early in the design process, but their exact proportions and placement may not be given. Simultaneously, their contributions to a ship's total resistance may be significant. It is therefore desirable to make accurate analytical estimates for their added resistance.

The added resistance of appendices and other hull modifications is difficult to determine from model tests. To achieve the correct inflow on the modifications, and assess the modifications' effect on the flow over the hull, it is not feasible to test them in isolation. They must be fitted on the actual hull. Unlike in full scale, the flow regime over the modifications may not be fully turbulent in towing tank tests[21]. This is due to the low Reynolds numbers. Resistance results will then not be fully scalable. Further, it is costly and time consuming to build and test multiple models with small variations.

A much used alternative to experimental tests is numerical simulation with computational fluid dynamics (CFD). Preoptimization with potential flow CFD was shown to reduce project duration already in the early 1990s[3]. While codes based on potential theory predict wave resistance quite well[15], their neglect of viscous effects is limiting. Viscosity is important only in the boundary layer, and the wake close to the ship, but the viscous resistance is often dominating[15]. With the increasing availability of computational resources, both researchers and industry have largely adopted viscous codes. Their computational demands are much larger, but they are more accurate than those based on potential flow. At the 2010 Gothenburg workshop for CFD, the mean error of all model scale resistance submissions was only $-0.1\%D$ [23], where D is the measured resistance. A downward trend for the standard deviation of errors was also shown, with a decrease to $2.1\%D$ from 4.7% in the 2005 workshop.

Model scale CFD is subject to the same scaling issues as towing tank tests. This can be solved by simulating in full scale. Despite increased simulation complexity from higher

Reynolds numbers[7], studies suggest comparable or better agreement with sea trials for full scale CFD than scaled model tests[29, 31]. However, due to measurement uncertainties it can not be conclusively confirmed. For direct comparison with sea trials, self-propulsion simulations are used. These types of simulations are attractive for final design validation, but they are overly time consuming for design phase predictions. Predicting vessel performance by way of hull resistance is therefore still of interest. In addition to the increased simplicity, accurate resistance results help ensure the quality of power-predictions[10].

2 Theory

2.1 Computational fluid dynamics

Computational fluid dynamics are the application of numerical approximations for the solution of fluid flow problems[13]. To numerically solve equations describing physical phenomena, the solution domain must be divided into a finite number of solution points, and the equations converted into a set of discrete algebraic equations. This is called discretization. Fluid flow varies in both space and time, and the solution at each point is dependent on neighboring solutions in both these domains.

In this study, a finite volume method is applied. This means that the points take the form of subdomains called cells, and the flow of the fluid through these is modeled. The terms grid and mesh are used interchangeably to describe the distribution of the cells.

Numerical results are always approximate. Approximations happen in

1. the mathematical modeling

2. the discretization

3. the application of iterative solution methods

Modeling errors

The modeling error is the difference between reality and the exact solution of the applied mathematical model[13]. Fluid flow is described mathematically by the Navier-Stokes equations. They are an equation set based on the continuity of mass, momentum and

energy. See for example Ferziger, Perič and Street[13] for their derivation and discretization.

The Navier-Stokes equations are considered to describe fluid flow exactly. Given unlimited computational resources, solutions of any desired accuracy can be achieved by solving them directly. However, this is generally not feasible. The biggest difficulty in numerically solving the equations is turbulence. It is computationally demanding, and requires very fine discretization to capture accurately. Turbulence modeling is discussed in Section 2.1.1.

Additional simplifications of importance are the free surface model, the use of wall functions, and the way ship motions are resolved. They are discussed in Sections 2.1.2 to 2.1.4. The use of boundary conditions to artificially make a finite volume infinite is also a potentially large source of error, but it can to some degree be controlled for. See Section 3.2.3.

Further, the flow is assumed isothermal and incompressible, meaning that the fluid's temperature, density and viscosity are modeled as constant. Incompressibility is in reality a property of a given fluid, but at the given velocities water may safely be assumed incompressible. Temperature variations within the domain are also deemed negligible. Minor inaccuracies may also stem from non-exact properties of the fluid.

The size of some modeling errors, such as the location of the far-field boundaries and the turbulence quantities, can be evaluated by varying their input parameters[13]. How much the solution varies from changes in these inputs then indicates the penalty of getting them wrong.

Modeling errors can also be quantified by comparing numerical solutions to experimental results. In the context of CFD, this is named validation[33]. As discussed in Chapter 1, CFD in model scale has been shown to consistently predict the calm water resistance accurately. Results from full scale self-propulsion studies also suggest that the approaches scale well. However, even with data on the real flow, modeling errors can not be determined exactly. They can only be estimated[13]. Modeling and numerical errors may cancel each other, causing numerically imprecise solutions to fit the experimental data

better. It is therefore only meaningful to validate a solution after the numerical errors have been estimated and deemed small enough. The estimation of iteration and discretization errors is named verification[33].

Discretization errors

The discretization error is the difference between the exact solution of the mathematical model, and the exact solution of the system of algebraic equations that results from the discretization[13]. For the finite volume method, surface, volume, and time integrals are approximated through discretization. Solutions are found only on discrete points in each cell. The number of discretization points affect not only where a solution is found, but also the flow physics. With insufficient resolution, the solution at each point will differ from reality. As the discretization size in space and time becomes smaller, the solution becomes a more accurate approximation. However, the computational effort is proportional to the number of points. Trade-offs must therefore be made between solution accuracy and solving time.

At intermediate locations between cell centers, flow values are determined by interpolation. This means that, if the changes in variables are small, only a few big cells are needed for an accurate solution. However, if solution gradients are steep, the number of cells must be high. This motivates the use of unstructured grids with local refinements. If certain characteristics of the solution are known beforehand, cells may be packed densely only in certain areas. Due to the complexity of a hull form, unstructured grids are also much easier to adapt to the geometry. The downside of these grids is an irregularity in the data structure, resulting in slower solutions than for structured grids[13]. Accuracy is not necessarily affected.

The size of the discretization error is estimated by systematic variations in the cell sizes. This is described in Section 2.1.5.

Iteration errors

The iteration error is the difference between the exact and the iterative solutions of the system of algebraic equations[13]. Discretization produces a set of non-linear equations. These are linearized and then solved iteratively. An iterative solution is based on making an initial guess for the solution, and then improving it systematically. If the solution converges, it will approach the exact result. However, since the number of improvement cycles must be finite, an error will always remain.

When to stop the iterations is determined by one or more convergence criteria. Tracking residuals is common for steady problems. This roughly means to stop the simulation when changes between solution steps are small. When steady solutions can not be achieved, outer iteration residuals will not converge. Then parameters of the solution must be considered to determine convergence.

Most interesting is the the relative size of the iteration error when compared to that of the discretization. This means that a coarser mesh allows for a larger iteration error than a finer one. Given convergence towards appropriate criteria, the iteration error is in any case assumed small compared to the discretization error[12].

2.1.1 Turbulence modeling

Turbulence is the interaction of time-varying vortexes of different sizes within fluid flow. To capture these vortexes when solving the Navier-Stokes equations numerically, a very high discretization fidelity is necessary. By using a simplified model for the contribution of the vortexes, and solving the equations directly only for the time-averaged fluid velocity, a coarser grid can be applied. The result is then not an instantaneous turbulent solution, but an averaged numerical one.

Mathematically, this is done by decomposing the velocity in Navier-Stokes into a time-averaged and a time-varying part. The resulting equations are named the Reynolds averaged Navier-Stokes equations (RANSE). This decomposition isolates the contribution of the time-varying velocities within an extra term in the momentum equations. This

term is called the Reynolds stress tensor. To solve the equations, closure between the stress tensor and the fluid velocity must be achieved. A widely used closure is the Boussinesq hypothesis. It provides the Reynolds stress tensor from the gradient of the mean velocity field[34]. An implicit assumption is then that the turbulent mixing length is small compared to the scales of which mean flow quantities vary. The validity of the Boussinesq hypothesis has been demonstrated, from both direct numerical simulation (DNS) and experimental data, to be limited[34]. However, two-parameter turbulence models based on it are currently dominating within computational ship hydrodynamics, and shows consistently accurate results for model scale ship resistance[23].

The two-parameter models add two more transport equations which must be solved simultaneously with the continuity and momentum equations. They are largely divided between two groups, k-ϵ and k-ω. Models of k-ϵ type have shown satisfactory accuracy in most of the flow, but lacks accuracy in the viscous sub-layer of boundary layer flows compared to k-ω[25]. The problem with regular k-ω is its large sensitivity to boundary values. An alternate formulation is the k-ω SST model. It is designed for accurate prediction of flows with strong adverse pressure gradients and separation[25]. This makes it popular in marine hydrodynamics. It applies the k-ω model in the viscous sublayer, but switches to k-ϵ based on wall distance.

These turbulence models are based on empirical approaches[24]. They are calibrated with DNS and experimental data on simple flows, such as flat plate boundary layer, shear layer, and isotropic decaying turbulence downstream of screens[41]. This increases their qualitative accuracy for given flows, but they can not be assumed universal.

2.1.2 The free surface

The free surface is an interface between two immiscible phases, namely water and air. Modeling the interaction between these fluids is necessary to accurately describe surface flows. Multiphase flow is difficult to describe exactly, and free surface flows are deemed a particularly difficult class due to the moving boundaries [13]. Resolving the free surface is a key complication for application of CFD in the marine field[14]. Its position is not known

beforehand, so it must be found as part of the solution process. Due to nonlinearities and stochastic behavior, this is no easy task.

There are two categories of methods for predicting the movement of an interface between immiscible fluids. They are interface-tracking and interface-capturing. For the first, only one phase is simulated. The grid moves and deforms with the free surface. This category is generally limited to simple interfaces, as the methods struggle with changes in interface topology[28]. With the second category, both phases must be modeled. A fixed grid is used, meaning that near-interface cells can be partially filled with each of the two phases. An additional equation must be added to the solver for determination of fluid distribution. When the volume fraction of one fluid is determined at a location, the fluid properties can be calculated. The most popular techniques for resolving the free surface are Volume of Fluid (VOF) methods[23]. They are in the interface-capturing category. VOF methods are computationally expensive, but have been proven robust in several cases[14].

A major disadvantage is that VOF methods are prone to numerical diffusion[28]. It is caused by errors accumulating while solving for the volume fractions. The bounding of the volume fraction between one and none is also a source of error, as most second-order (and higher) schemes produce over- and undershoots. A third problem is that only volume fractions within cells are solved for, not the exact free surface. This means that the free surface profile isn't sharply defined. It is smeared. Local grid refinement is therefore important for accurate resolution. Ideally, the grid should be refined until all cells contain only one phase[13]. In Star-CCM, an extra scheme named High-resolution interface capturing (HRIC) is applied with VOF. It suppresses numerical diffusion and helps predict sharp interfaces[22].

2.1.3   Ship motions

When a vessel moves through calm water, displacement forces will cause it to sink and trim. Sinkage is vertical translation, while trim is rotation around the transverse axis. Corresponding dynamic motions are heave and pitch.

Sink and trim motions are generally small, but they change the pressure field[22]. This

affects the resistance, and they are therefore important to predict accurately. To resolve them, Star-CCM implements a method named Dynamic fluid body interaction (DFBI).

When running calm water simulations in Star-CCM, the ship's volume is not discretized. Only its surfaces are modeled. This means that there is no vessel body that can sink and trim. Instead the entire computational domain must be moved during simulations. The vessel surfaces are included as boundaries of the fluid mesh. Forces and moments are calculated at this coupled boundary, and the mesh is moved correspondingly. With DFBI, the fluid mesh is moved rigidly[36]. This means that the relative distances between internal points of the grid do not change.

Accurate CFD predictions for sinkage and trim have generally not been achieved. Both show comparison errors and standard deviations larger than those for resistance[23]. It is speculated that this is simply due to the difficulties in measuring the quantities at the low velocities for which current test cases have been investigated, or due to the variables' dependence on accurate free surface deformation[23].

2.1.4 Wall functions

In viscous fluids, such as water and air, fluid particles at a solid surface will have a zero relative velocity. When a vessel advances in water, this means that the water particles on the hull surface will have the same velocity as the vessel. Adjacent particles will then experience shear forces from this innermost layer, but will resist deformation to some degree. This results in a wall normal velocity profile that approaches the free stream velocity with increasing distance from the surface. The affected region is called the boundary layer.

In a full scale ship resistance simulation, accurately resolving the boundary layer requires infeasibly small cells near the hull surface. Both experiments and direct numerical simulation of Navier-Stokes have shown that, for a wide number of geometries, the tangential fluid velocity near a surface can be accurately modeled analytically[13]. These analytical models are named wall functions. They are based on the boundary layer approximation. This means that they assume no reversed flow, no recirculation, and that the variation of

the geometry is gradual[13]. This occurs in channels and pipes, and over mildly curved solid walls such as a ship hulls. While a real turbulent boundary layer is unsteady, with an instantaneous velocity profile that varies in time, the wall functions provide only time-averaged values.

When discussing wall functions, the notation n^+ (or y^+) is used to describe the normalized normal distance from the wall. Its definition is given in Equation (2.1),

$$n^+ = \frac{n u_\tau}{\nu}, \tag{2.1}$$

where n is the normal distance from the wall, ν is the kinematic viscosity, and u_τ is the friction velocity defined in Equation (2.2).

$$u_\tau = \frac{\tau_{wall}}{\rho}. \tag{2.2}$$

τ_{wall} is the wall shear stress determined from Equation (2.3).

$$\tau_{wall} = \frac{1}{2}\rho U^2 C_{f,x}. \tag{2.3}$$

$C_{f,x}$ is the local skin friction coefficient.

Accurate analytical descriptions for the tangential fluid velocity exists for two regions of the boundary layer. The first is the viscous sublayer, where the velocity profile varies linearly[13]. It corresponds to n^+ values lower than 5. The second is the logarithmic region, which starts at an n^+ of 30. Its upper limit is less clearly defined, but an n^+ of 200 is often suggested. A formulation of the log-law is given in Equation (2.4),

$$\frac{1}{\kappa}\ln(n^+) + B, \tag{2.4}$$

where κ and B are empirically determined constants. It is not strictly valid for flow over complicated wall shapes[13], but it has been shown to be applicable for nearly all wall-bounded boundary layers[41].

Between the linear and logarithmic regions, different blending functions are in use. Their accuracy is less certain, and the general recommendation is to avoid this range when determining tangential fluid velocities analytically.

11

2.1.5 Grid convergence studies

Discretization errors and uncertainties are determined by monitoring the change in solution quantities during systematic grid size variations. Monitored quantities can be either direct solution variables such as velocities and pressure, or integral quantities such as body drag[13]. Convergence studies must be conducted for all quantities of interest, since the order of convergence may vary between them.

The starting point for discretization error estimation is Richardson extrapolation. It requires three grids of varying fidelity with a constant refinement ratio r. The grid fidelity is measured by a characteristic grid size h. All three grids must be sufficiently fine for the quantity to converge monotonically towards an extrapolated solution.

First, the convergence rate p is determined by Equation (2.5),

$$p = \frac{\log\left(\frac{\phi_{h_2} - \phi_{h_1}}{\phi_{h_3} - \phi_{h_2}}\right)}{\log(r)}, \tag{2.5}$$

where $h_1 < h_2 < h_3$, and ϕ_{h_i} is the quantity of interest at grid level h_i. The discretization error at grid h_i can then be estimated by Equation (2.6).

$$\epsilon_{h_i} = \frac{\phi_{h_i} - \phi_{h_{i+1}}}{r^p - 1}. \tag{2.6}$$

For unstructured grids with uneven refinement, achieving a constant refinement ratio is not straightforward. A method based on generalized Richardson extrapolation that handles uneven refinement is the Grid-Convergence Index (GCI)[32]. It is recommended by Journal of Fluids Engineering (JFE)[8], and is here presented by their definition.

The GCI definition of characteristic grid size is given in Equation (2.7),

$$h = \left(\frac{1}{N}\sum_{i=1}^{N}(\Delta V_i)\right)^{\frac{1}{3}}, \tag{2.7}$$

where N is the number of cells, and ΔV_i is the volume of cell i.

Due to the non-constant refinement ratios

$$r_{21} = \frac{h_2}{h_1} \neq r_{32} = \frac{h_3}{h_2},$$

the apparent order p is found by iteration. Once the apparent order is found, the extrapolated solution is given by Equation (2.8).

$$\phi_{ext} = \frac{r_{21}^p \phi_{h_1} - \phi_{h_2}}{r_{21}^p - 1}. \tag{2.8}$$

It is an estimate for what value the quantity will take at an infinitely fine grid.

The relative uncertainty GCI of the fine grid solution is given in Equation (2.9),

$$GCI = F_S \left| \frac{\epsilon_{h_1}}{\phi_{h_1}} \right|, \tag{2.9}$$

where $F_S = 1.25$ is an empirically determined safety factor. This is not a statistically well founded error estimate, but it is argued that it can be interpreted similarly as the two-sigma limit[32]. This is understood to mean that the converged solution lies within $(1 \pm GCI) \times \phi_{h_1}$ with a 95% confidence level.

With the three grid GCI method, only a single instance of p is given. This makes it highly sensitive to small disturbances in monitored values. and thus unreliable for noisy data. In grid convergence studies, noise can stem from lacking geometrical similarity between grids of different refinement levels, flux limiters used in the discretization of convective terms, damping functions, and switches in turbulence models[12]. To remedy this, the use of least squares curve fitting with a minimum of four grids to approximate the order of convergence has been suggested[12]. Least squares curve fitting means to find the parameters for a function $f_\phi(h)$ that minimizes Equation (2.10),

$$\sum_{i=1}^{n_g} w_i (f_\phi(h_i) - \phi_{h_i})^2, \tag{2.10}$$

where n_g is the number of grids, and w_i is the weight of the solution at grid i.

The method assumes that the CFD code is theoretically second-order accurate. Variations of Equation (2.11) are used for f_ϕ.

$$f_\phi(h) = \phi_{ext} + \alpha h^p. \tag{2.11}$$

First, the order of convergence p is found by least squares fitting Equation (2.11) to the data with and without weights. The weights are determined from the characteristic grid

size defined in Equation (2.7), meaning that results from finer grids are assumed more accurate. For the unweighted fit, w_i is set equal to 1. If only one fit shows an order of convergence between 0.5 and 2, then this fit is used. If both do, the fit with smallest standard deviation is chosen.

If neither of the two fits are within the desired range, they are discarded. Instead weighted and unweighted fits based on first and second order convergence are made. p is then respectively set to 1 and 2 in Equation (2.11), and values only for ϕ_{ext} and α are found. If p is less than 0.5 in both the discarded fits, additional weighted and unweighted mixed first and second order fits are made. Of the four (or six) fits, the one with the smallest standard deviation is chosen.

Once the best least squares fit has been selected, the discretization uncertainty at h_i is determined based on the spread in data $((\phi_{h_i})_{max} - (\phi_{h_i})_{min})$, the estimated discretization error at this point, the standard deviation of the least squares fit, and the difference between ϕ_{h_i} and $f_\phi(h_i)$.

2.2 Ship resistance

Ship resistance consists of two parts, pressure and friction[26]. They describe normal and tangential forces on the hull, respectively. Friction stems purely from the viscosity of the fluids that the ship advances through. Pressure resistance results mainly from wave making. William Froude (1810 - 1879) showed that the inviscid wake making resistance and viscous frictional effects can be largely separated, and that the inviscid drag can be scaled by the Froude number. However, the pressure resistance also has a viscous part which interacts with the wave making resistance. This is not accounted for when Froude scaling, and is a widely recognized disadvantage of the method[31]. The friction and viscous pressure components are Reynolds number dependent.

For ships, the total drag R_T is non-dimensionalized by Equation (2.12),

$$C_T = \frac{R_T}{0.5\rho V_S^2 S_S} \tag{2.12}$$

where C_T is the total drag coefficient, V_S is the vessel velocity, and S_S is the wetted

surface of the hull. When considering the two resistance components separately, they can be non-dimensionalized similarly. R_T is simply replaced with the relevant component.

The viscous resistance can be estimated based on regression analyses. An often used regression is the ITTC'57 correlation line, given in Equation (2.13),

$$C_F = \frac{0.075}{(\log_{10}(Re) - 2)^2},$$
(2.13)

where Re is the Reynolds number.

Equation (2.13) gives the friction resistance of a flat plate, and assumes a zero pressure gradient along it[40]. For a hull form, this assumption does not hold. To find the friction resistance of a ship, C_F is multiplied by $(1+k)$, where k is a shape dependent form factor. The form factor is a measure of the increased frictional resistance caused by displacement effects[39]. It is assumed constant for all velocities, though multiple studies show that it is both Froude and Reynolds number dependent[29].

The drag resistance F_D of an arbitrary object can be described by Equation (2.14),

$$F_D = C_D S \rho V^2,$$
(2.14)

where C_D is an assumed constant drag coefficient, S is the object's wetted surface, ρ is the fluid density, and V is the velocity of the fluid relative to the object.

For ship appendix, the drag coefficient is not assumed constant. Therefore, ITTC suggests Equation (2.15) is used instead[18],

$$R_{App} = 0.5\rho V^2 C_F (1+k) S_{App},$$
(2.15)

where V is the relative velocity of the appendix compared to the water, C_F is the friction coefficient of the appendix, and k is its form factor.

The hull shape displaces water as it advances, meaning that an appendix may not experience the same fluid velocity as the hull. Particularly aft mounted appendices are affected by this. The relative velocity of the appendix compared to the water is described by the wake fraction w. It is a measure of the relative velocity of the water compared to the

ship hull at an observation point. See Equation (2.16),

$$w = \frac{V_S - V_{Observed}}{V_S},$$ (2.16)

where V_S is the vessel velocity. The wake fraction is assumed constant for a given point on a hull shape, meaning that $V_{Observed}$ can be determined at a given V_S without new measurements. In Equation (2.15), this means that V must be replaced by $(1 - w)V_S$.

Added resistance from lateral tunnels depends on the tunnels' placement. Even though yard experience suggests it is negligible for bow tunnels[35], several analytical expressions for its determination exists. The cited source likely refers to large ships with small tunnels. Tunnels contribute mainly to the pressure drag, and the assumption of a constant drag coefficient is applied. The tunnels are a modification of the hull. They have no clearly defined surface of their own, but expressions are based on their cross-sectional area. Holtrop's method [5] gives the total tunnel resistance R_{TH} by Equation (2.17),

$$R_{TH} = \rho \pi V^2 d_{TH}^2 C_{D_{TH}},$$ (2.17)

where d_{TH} is the tunnel diameter, and $C_{D_{TH}}$ is the tunnel drag coefficient. The method suggests tunnel drag coefficients in the range 0.003 to 0.012, depending on tunnel placement and hull curvature. The lower range is for tunnels placed on the bulb near the bow, where the hull surface is near parallel to the flow.

In Hollenbach's method[5], Equation (2.18) is used for estimation of the tunnel drag coefficient,

$$C_{D_{TH}} = 0.003 + 0.003(\frac{10d_{TH}}{T} - 1),$$ (2.18)

where T is the vessel draught.

Stuntz[4] proposes Equation (2.19) for predicting duct resistance,

$$R_{DUCT} = \frac{0.07\rho}{2} A V_S^2,$$ (2.19)

where A is the duct cross sectional area. Rewriting it to the form of Equation (2.17) gives a corresponding tunnel drag coefficient $C_{D_{TH}}$ of 0.00875, which is near the middle of Holtrop's range. Christensen[9] suggests $C_{D_{TH}} = 0.00174592$.

3 Method

3.1 Geometry

The investigated ship is an offshore supply vessel (OSV) with two sequential bow thrusters and headboxes for the mounting of thrusters. The hull is visualized in Figures 3.2 and 5.2.

The vessel's length is in the 50 to 100 meter range. At the tested draught, the block coefficient C_B is 0.621. The tunnels have identical diameters, and their openings have chamfered edges. The headboxes have foil shaped cross sections. Due to confidentiality, more detailed descriptions can not be given.

3.2 Computational setup

Simulations are performed in Star-CCM+ 2019.3, a commercial CFD software package released by Siemens. The problem is modeled as transient, with a first order, implicit unsteady time integration scheme. This makes the solution unconditionally stable. Transport equations are handled by a segregated flow model, applying a second order upwind scheme for convection. Details of the setup are described in the following subsections.

3.2.1 Flow discretization

As discussed in Section 2.1, necessary cell distribution depends on velocity and pressure gradients. These gradients are expected to be large near the vessel surface, and in the kelvin wake[13]. Grid refinements are therefore applied in these regions. As the free surface is resolved with a Volume of Fluid approach, a fine mesh is also required across
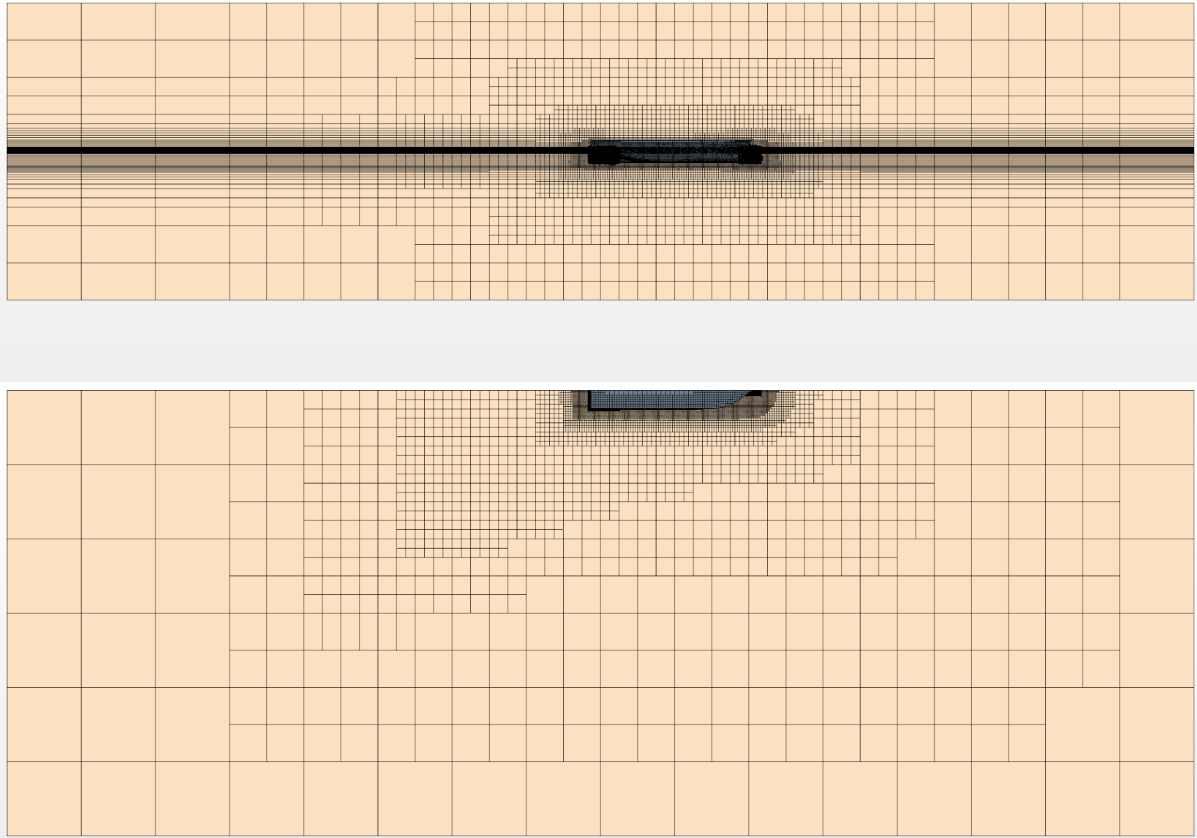
Figure 3.1: Domain mesh overview for coarsest grid (full scale, h=3.7).

the water/air boundary to accurately resolve the interaction of the fluids.

The domain mesh is a regular hexahedral cell mesh aligned with the flow direction. For cell boundaries to intersect correctly, the minimum growth rate is doubling of the cell side length in one or more directions. Three layers of mesh refinements are used for each of the three critical regions defined above. As the wake refinements completely surround the hull boxes, there are six levels of mesh refinements between the domain boundaries and the near hull flow. A seventh level is applied around the bow, stern, tunnels and headboxes. An overview of the discretized domain is shown in Figure 3.1.

Due to the complex geometry of the hull, an unstructured prism layer mesh is used near the hull surface. This mesh is fitted within the domain mesh by trimming adjacent cells, turning them polyhedral. Outer prism layer cells are of similar size as the innermost

domain cells. The prism cells then decrease in thickness with a geometric progression towards the hull surface. Their length is determined from the domain mesh, and is constant through all layers. An impression of the prism cell distribution is given by Figure 3.3.
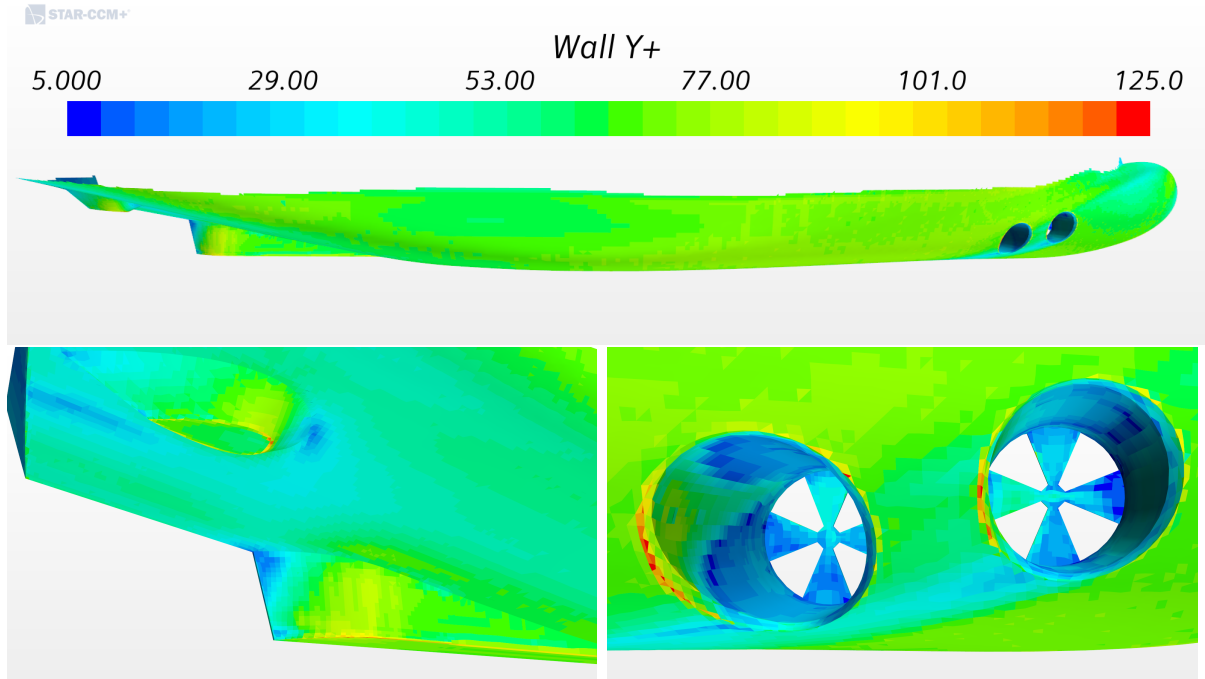
Figure 3.2: Distribution of n^+ values over the submerged hull.

In addition to mentioned geometry concerns, the prism layer mesh is necessary to capture the steep gradient of the flow velocity in the boundary layer. As discussed in Section 2.1.4, the near hull fluid velocity can be accurately determined with wall functions given innermost computation points in the logarithmic region. The International Towing Tank Conference (ITTC) recommends an n^+ range of 30 to 100[19]. The upper bound appears less important than the lower, with examples from the literature of n^+ values of several hundreds for full scale simulations[31, 20]. Target n^+ is here set to 60. This gives a distribution as shown in Figure 3.2.

The near wall prism layer thickness is set based on the one-seventh-power law[41]. It is a simplified method, assuming Equation (3.1) to hold,

$$\frac{u}{U} = \left(\frac{n}{\delta}\right)^{\frac{1}{7}},\tag{3.1}$$

where u is the flow velocity parallel to the wall, U is the parallel free stream velocity, n is the normal distance from the wall, and δ is the normal position of the boundary layer edge.

Equation (3.1) gives a local skin friction coefficient $C_{f,x}$ for a smooth plate as in Equation (3.2)[41].

$$C_{f,x} = \frac{0.027}{Re_x^{\frac{1}{7}}}. \tag{3.2}$$

$C_{f,x}$ is used to find the wall shear stress with Equation (2.3). With known wall shear stress, the friction velocity can be found with Equation (2.2). Finally, the normal distance from the wall at which n^+ takes the desired value is determined by Equation (2.1).

Exact n^+ values can only be found by performing simulations. With the mentioned target n^+ of 60, for all full scale simulation results, the largest mean n^+ value over the submerged hull is 66.6. The lowest is 59.8. In model scale the maximum and minimum mean values are 65.8, and 55.9, respectively. The near wall cell heights are therefore not adjusted from the one-seventh-power law estimate.

3.2.2 Time step

The time step is set by the convective time scale τ. It is defined in Equation (3.3),

$$\tau = \frac{L}{V}, \tag{3.3}$$

where L is the characteristic length of the simulated model, and V is the fluid velocity. The length between perpendiculars has here been used for the characteristic length L. When using two-equation turbulence models, ITTC recommends using time steps smaller than 0.01τ[19].

3.2.3 Computational domain

The goal of each simulation is to find the resistance of a vessel in infinite, undisturbed still water. In practice, this means that interaction between fluid and boundaries should not affect the results. Star-CCM implements no non-reflective boundary options[36], and damping is thus necessary for any reasonably sized domain.

Discretization errors introduce some damping [13]. The occurrence of wave reflections is therefore limited by the coarse mesh near the boundaries. However, this is insufficient, and Star-CCM's wave damping model is applied. This model's damping zone is limited to extend equally from all boundaries it is applied to. Siemens recommends that the damping zone extends into the first mesh refinement, and that there are at least two ship lengths between the hull and damping boundaries. A damping length of $2 \times Lpp$ is therefore applied for the simulations, excepting the two lowest velocities. For them, the damping length is increased by 5 and 10 percent, to improve solution stability. At lower velocities, the extension of the wake from the hull is smaller, so this is not expected to affect solution accuracy.

With necessary sizes of mesh refinement volumes already determined, the domain size is largely given from the requirements for numerical wave damping. Domain dimensions of $(-4Lpp < x < 4Lpp, 0 < y < 3Lpp, -Lpp < z < Lpp)$ are used, with the origin on (aft perpendicular, central axis, waterline), as shown in Figure 3.1. This domain is longer and wider than those used for most comparable studies. It is more shallow than some recommend[16], but the chosen depth is not without precedence[31, 20]. To ensure that the damping is sufficiently effective, time histories of wave cuts at four distances from the hull are stored and animated to look for any signs of wave reflections.

For the boundary conditions, velocity inlets are used at domain front, top and bottom. At velocity inlets, velocity properties must be prescribed. The exact solution of the flow must therefore be known at their location for the duration of the simulation. Symmetry planes are placed both along the vessel's central axis and the outer domain wall. Here the normal velocity, and the gradient of all other variables are set to zero. There is zero flux across this boundary and there is no tangential shear stress[36]. Downstream from the ship, the boundary is specified as a pressure outlet. At the pressure outlet, velocity is extrapolated from the domain interior. However, the static pressure of the environment outside the simulation domain must be prescribed[36]. Vessel surfaces are also modeled as domain boundaries. They are set to no-slip walls. On wall boundaries, the fluid velocity is zero. This equals the velocity of the simulated vessel, as there is in actuality no vessel

advancing through the domain. Instead the fluid flow passes through the domain in which the vessel is held stationary.

3.2.4   Turbulence model

Turbulence is modeled with the k-ω SST turbulence model mentioned in Section 2.1.1, due to its availability and popularity in the literature. It has been thoroughly tested[25], and applied for both full and model scale ship simulations[7, 16, 20, 31].

k-ω SST is a two-parameter model, and so requires that two free stream turbulence parameters are prescribed at the domain boundaries. These are the turbulent kinetic energy k, and the specific rate of dissipation ω. In Star-CCM, these parameters can be defined from their relation to the turbulence intensity, which is a measure of how much turbulence is in the free stream, and the viscosity ratio, which is the ratio of turbulent to laminar viscosity.

In calm water, the flow is undisturbed or weakly turbulized. By definition, the flow is weakly turbulized if the turbulence intensity is smaller than 1% [27]. Thus, the Siemens recommended value of 1%[36] is used on all inflow and outflow boundaries. The viscosity ratio is set to the default value of 10 without further investigations.

Flow turbulence over a ship hull is affected by surface roughness. A real ship will never be perfectly smooth, and the surface roughness will increase during its life span from erosion and marine growth. The exact roughness is therefore hard to emulate geometrically. It is also computationally demanding to simulate. For these reasons, hull roughness is not considered.

3.2.5   Ship motions

The equilibrium version of the DFBI model mentioned in Section 2.1.3 is activated to resolve ship trim and sinkage. It is a pseudo-steady approach, displacing the mesh by increments to an actively updated equilibrium position estimate. Force monitors are set to log only when forces are within the models equilibrium criteria. An equilibrium

model is expected to give equivalent results as a free motion approach, but with faster convergence[36]. The model is dependent on the vessel's mass, center of gravity, and moment of inertia around the transverse axis.

Both mass and center of gravity are determined from a high fidelity discretization of the submerged hull. Discretized volume multiplied by water density gives the mass, while the longitudinal center of buoyancy (L.O.B) is found as mean distance of the cells from the aft perpendicular. As an even keel load condition is assumed, the center of gravity is placed on the vessel's central axis, with a longitudinal position equal to L.O.B.

An exact calculation of the moment of inertia requires precise knowledge of the vessel's mass distribution for a given load condition. However, given that the moment of inertia is within reasonable limits, it will affect only how the vessel approaches its equilibrium trim position, not the trim angle itself. A rough estimate is therefore deemed sufficient. The longitudinal radius of gyration can be approximated by $K = 0.25 L_{pp}$[2]. The moment of inertia is then given in Equation (3.4),

$$I_{yy} = K^2 m, \tag{3.4}$$

where m is the vessel mass.

3.3   Grid convergence study

Discretization errors are estimated by systematically refining the grid. This is not straightforward for unstructured grids with local refinements. Consistent rules for grid refinement must be defined. Here, three main grid sizes are used. The coarsest has maximum cell sizes of $0.5 Lpp$ near the boundaries. The trimmed cell mesh size is then halved between cases.

For the prism layer mesh, the thickness of the first prism layer must be kept constant. k-ω SST predictions of viscous resistance have been shown sensitive to the near wall cell height when using wall functions[30]. This is regarded as a modeling error. To isolate grid uncertainties, keeping this error constant between refinements is desirable.

Further, to achieve geometrical similarity between grids, the total thickness of the prism layer mesh is kept constant. Therefore, only the number of prism layers cells is adjusted. The number of layers is determined from the transition between prism layer and trimmed cell mesh. The goal is to keep this transition smooth. This is not a perfectly consistent approach[10], but compliance with all requirements is not possible. The stretching ratio and total thickness of prism layers have been shown to have only a slight influence on results[30]. Refinement of the prism mesh between grids is shown in Figure 3.3.

(a) Full scale with h-values of 3.7, 2.1 and 1.1.
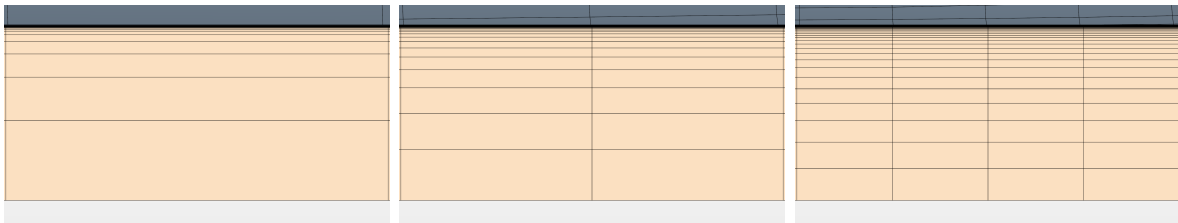
(b) Model scale with h-values of 0.34, 0.19 and 0.10
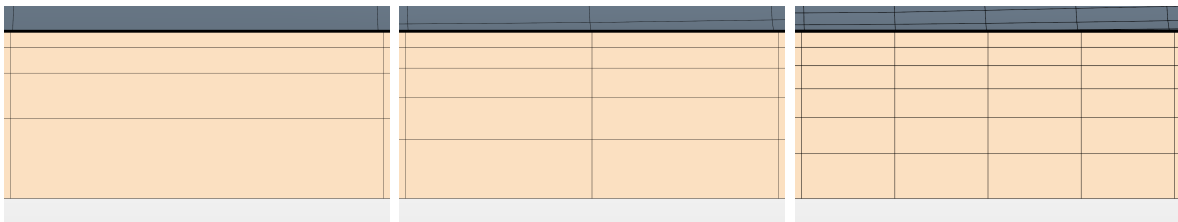
Figure 3.3: Refinement of the prism layer mesh

Grid refinement studies are conducted in both model and full scale at five velocities. The velocities correspond to Froude numbers 0.148, 0.185, 0.222, 0.250 and 0.296. In model scale, only the geometry with headboxes and bow tunnels is considered. In full scale, grid convergence is investigated for both the naked hull, and the hull modeled with headboxes and bow tunnels. This is to assess whether the less complex geometry of the naked hull can be accurately simulated on coarser grids than the appended one.

Discretization uncertainty is determined in two different ways. Both are described in Section 2.1.5, and implemented in Python. They are combined in a single convergence calculator class. It applies GCI when only three solutions are provided, otherwise least squares fitting. The implementation is provided with the thesis. An example use case and unit tests are provided as well. With GCI, the JFE provided[8] test data is used for

testing. For the least squares fitting method, code verification data is not provided with the approach description[12]. It is therefore tested only for simple cases, namely perfect linear, second, and half order convergence with zero noise. Least squares curve fitting is done using the *curve_fit* function of the Scipy module. It solves non-linear least squares problems with the *Levenberg-Marquardt algorithm as implemented in MINPACK* (from scipy.org).

When using the Grid-convergence Index method, only three grids are considered. To comply with demands for the least squares fitting approach, solutions for two intermediate grids are found when applying it. These grids have maximum cell sizes of $0.333Lpp$, and $0.167Lpp$, fitting in between the existing sizes of $0.5Lpp$, $0.25Lpp$ and $0.125Lpp$.

With an implicit solver such as here, a small time step is not necessary for convergence, but it is adjusted with the trimmed cell mesh size to largely keep its relative size equal between grids. In the bow and stern, where the flow is normal to the hull surface, this equality will break. This is because the prism layer mesh does not follow the same rate of refinement as the trimmed cell mesh. For the coarsest grid, the ITTC-recommended maximum time step of 0.01τ is applied[19], with τ defined in Equation (3.3). The mass and longitudinal center of gravity are kept constant for all levels of grid refinement.

3.4   Validation

Validation of model scale simulations is conducted by direct comparison to towing tank results. Experimental tests were conducted by Marintek (now Sintef Ocean) in 2012 on behalf of Havyard Design & Solutions.

Full scale simulations are compared to ITTC'78 scaled[18] experimental results. Marintek's formula for the form factor is used[29]. Since the simulated hull geometry is smooth, the surface roughness correction is not added. The air resistance of the superstructure is not included either, since the structure is not present on any of the geometries.

3.5 Time step convergence study

To determine the sensitivity of results on the time step, a time step convergence study is conducted. Calm water ship resistance calculations have been shown to not be particularly sensitive to the time step size[38], so a less rigorous approach than for grid convergence is applied. For the study, a single velocity is considered for each of a full and a model scale case. The chosen velocities correspond to Fn = 0.250 in both cases. Bow tunnels and headboxes are fitted on the geometries. The finest grids from Section 3.3 are applied, and the time step is varied from 0.04τ to 0.0025τ, halving it between each run.

3.6 Added resistance

Using the finest grids considered during grid convergence studies, the full scale hull is simulated with each modification separately. The time step is set to 0.005τ based on time step convergence results.

To find appropriate coefficients, analytical equations discussed in Section 2.2 are fitted to the data with least squares. The fits are weighted based on inverse discretization uncertainties. For the tunnel thrusters, results are compared to Stuntz's and Hollenbach's suggested parameters.

When using Equation (2.15) for headbox resistance, the wake fraction at headbox position is needed. To find the wake fraction, velocity probes are placed on the headbox position for simulations without it. Velocities are found for simulations with both tunnels and simulations without any of them. Probes are placed according to Figure 3.4, The water flow follows the hull at this location, and the headbox is angled towards the flow. Therefore, the mean velocity magnitude is used to calculate the wake fraction.
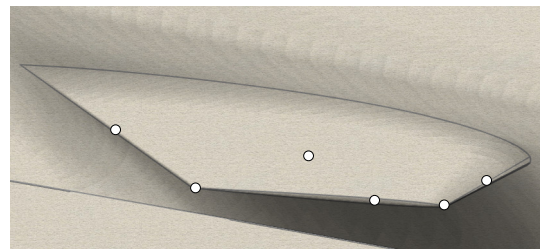
Figure 3.4: Position of wake fraction probes in the xz-plane. All probes are placed along the headbox centerline.
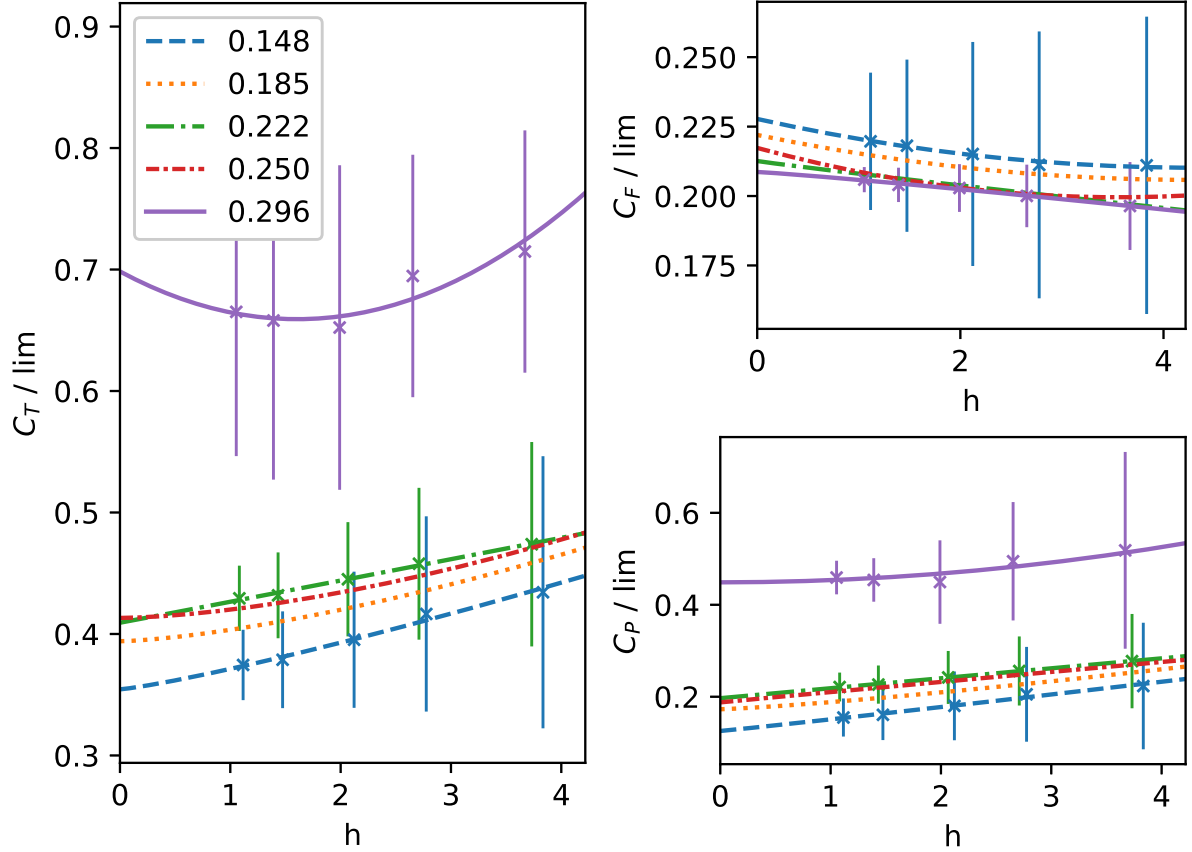
4 Results

4.1 Grid convergence
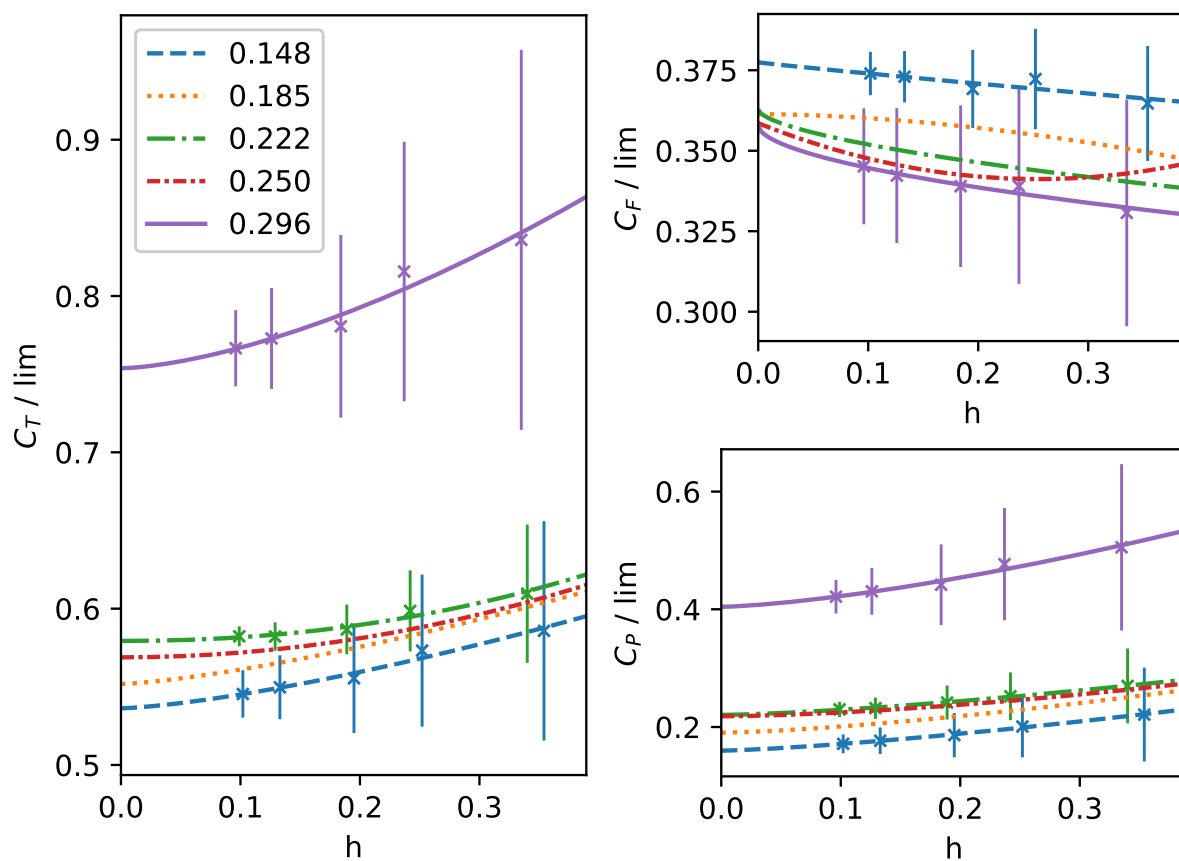
Figure 4.1: Mesh convergence of resistance for model scale vessel with headbox and transverse tunnels. Line labels state the Froude number.

Fitted resistance convergence curves are plotted in Figures 4.1 and 4.2. Due to confidentiality of absolute resistance values, they are scaled by an arbitrary limit. The limit is the same in all grid convergence plots, meaning that the ratios between total, friction, and

Figure 4.2: Mesh convergence of resistance for full scale vessel with headbox and transverse tunnels. Line labels state the Froude number.

pressure resistance coefficients are correct. So is the ratio between full and model scale results. Data points and discretization uncertainties are plotted only for select velocities to avoid overcrowding the figures. These are considered representative. Convergence curves for the resistance of the naked full scale vessel, and for vessel motions, can be found in Appendices A.1 and A.2.

With GCI, an order of convergence above 2 is found for 18 of 75 convergence cases. Among them total resistance convergence for 3 out of 5 velocities in model scale. 10 cases show an order of convergence below 0.5, none of them total resistance. The mean uncertainty for model scale total resistance is 0.6%. In full scale, this number is 3.4% with tunnels and headboxes and 2.0% without. Mean uncertainties for other parameters are generally higher, but the uncertainty spread between velocities is large.

With least squares fitting, mean relative uncertainty for model scale total resistance is 3.9%. For full scale, mean relative uncertainty of total resistance is 7.2% and 6% with and without tunnels and headboxes. All three values are heavily affected by the large uncertainty of the highest velocity. Without it, the three mean uncertainties are 3.0%, 5.5% and 4%, respectively.

All orders of convergence and discretization uncertainties are tabulated in Appendix A.3.

## 4.2   Time step convergence
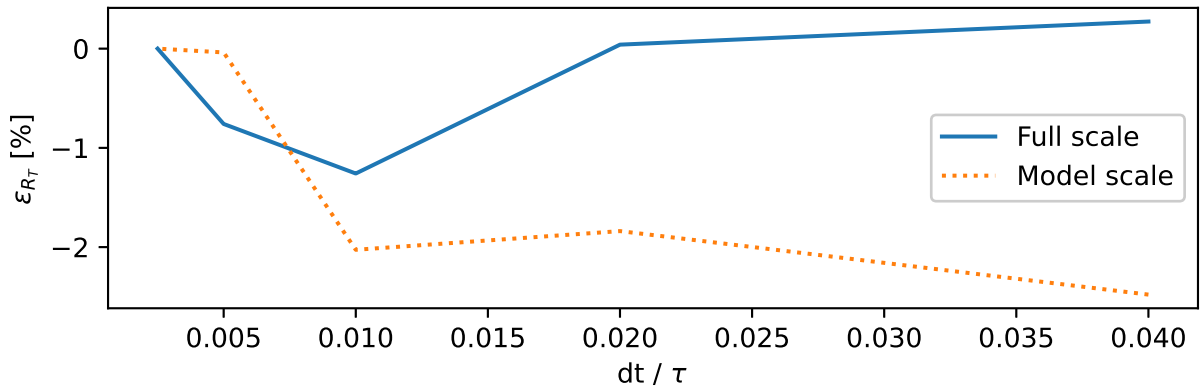
Figure 4.3: Time step convergence of resistance at Fn = 0.250. Results for $dt = 0.0025\tau$ are used as exact value.

Time step convergence results are plotted in Figure 4.3.

4.3   Validation

Model scale validation results are plotted in Figure 4.4. The mean errors over all Froude numbers for the finest grids are 0.2%, -7.7% and 7.7% for total resistance, sinkage, and trim, respectively. An underprediction for sinkage means that CFD predicts that the hull sinks deeper into the water compared to the towing tank tests.

For extrapolated results, the mean error for total resistance is -0.3% for the GCI method, and -1.1% for the least squares fittings. GCI overpredicts sinkage by 38%, and trim by 7.2%. Corresponding numbers for least squares fitting is -9.8% and 9.2%. The large

(a) GCI

(b) Least squares fitting
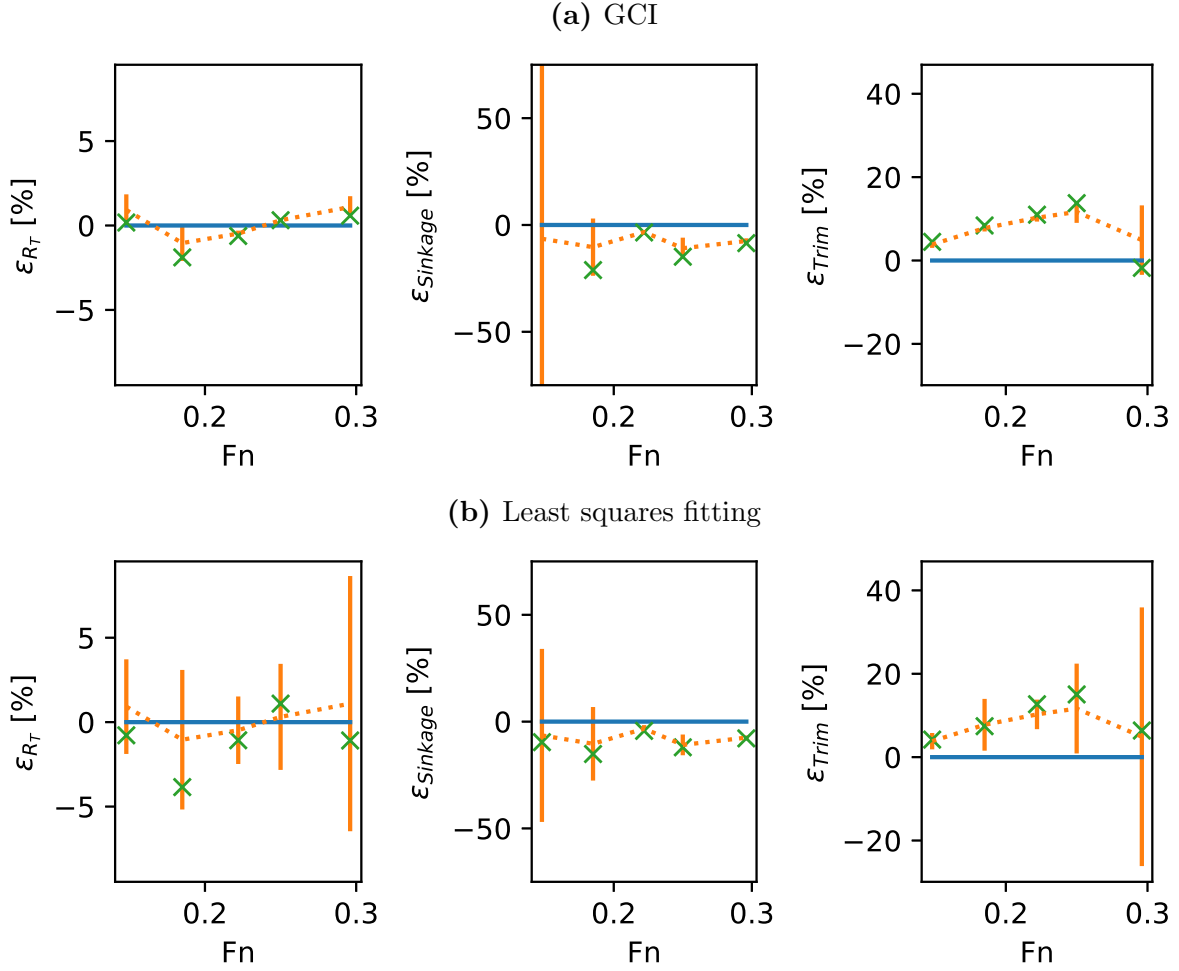
Figure 4.4: Percentage deviation for fully appended model scale CFD simulations from model test results with discretization uncertainties indicated as error bars. Fine grid solutions follow the stippled lines. X marks extrapolated results.

average overprediction of sinkage for GCI is caused by a massive overprediction at $Fn = 0.148$, where apparent order of convergence is near zero, and the relative uncertainty is 326%.

Full scale CFD values are compared with scaled towing tank results in Figure 4.5. Fine grid CFD predicts total resistance to lie on average 8.4% above the scaled model test. For respectively GCI and least squares fitting, extrapolated total resistance results are on average 5.7% and 4.7% above the scaled model test.
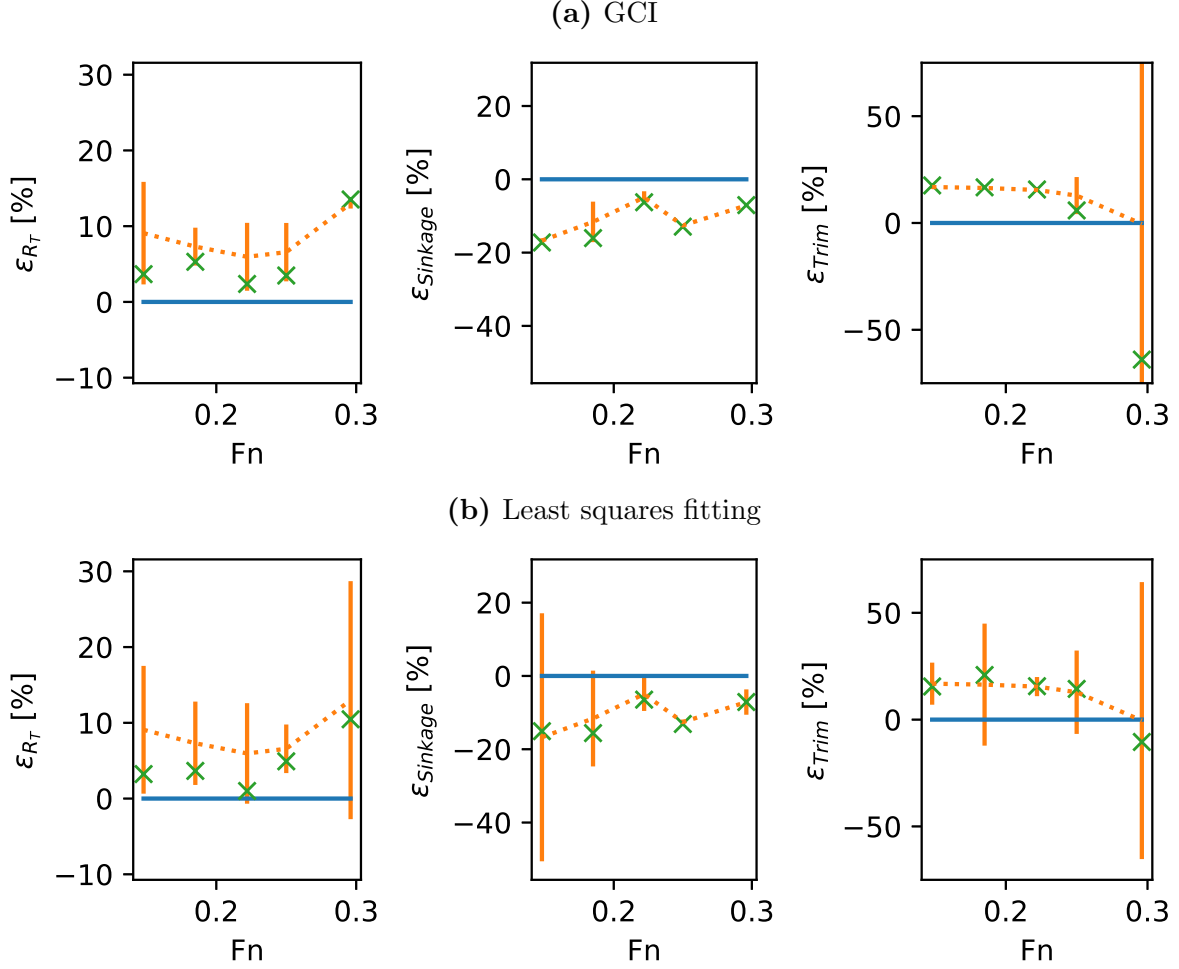
Figure 4.5: Percentage deviation for fully appended full scale CFD simulations from scaled model test results with discretization uncertainties indicated as error bars. Fine grid solutions follow the stippled lines. X marks extrapolated results.

4.4 Added resistance

The added resistance coefficient for different hull modifications in full scale are shown in Figure 4.6. For percentage added resistance instead, see Appendix A.4. In model scale, only the sum added resistance of both tunnels and headboxes are found. This sum can be seen as both added resistance coefficient and percentage change in Figure 4.7.

Using a weighted least squares fitting method on Equation (2.17), with weights determined from inverse discretization uncertainties, we find that $C_{D_{TH}}$ is 0.0055 for tunnel
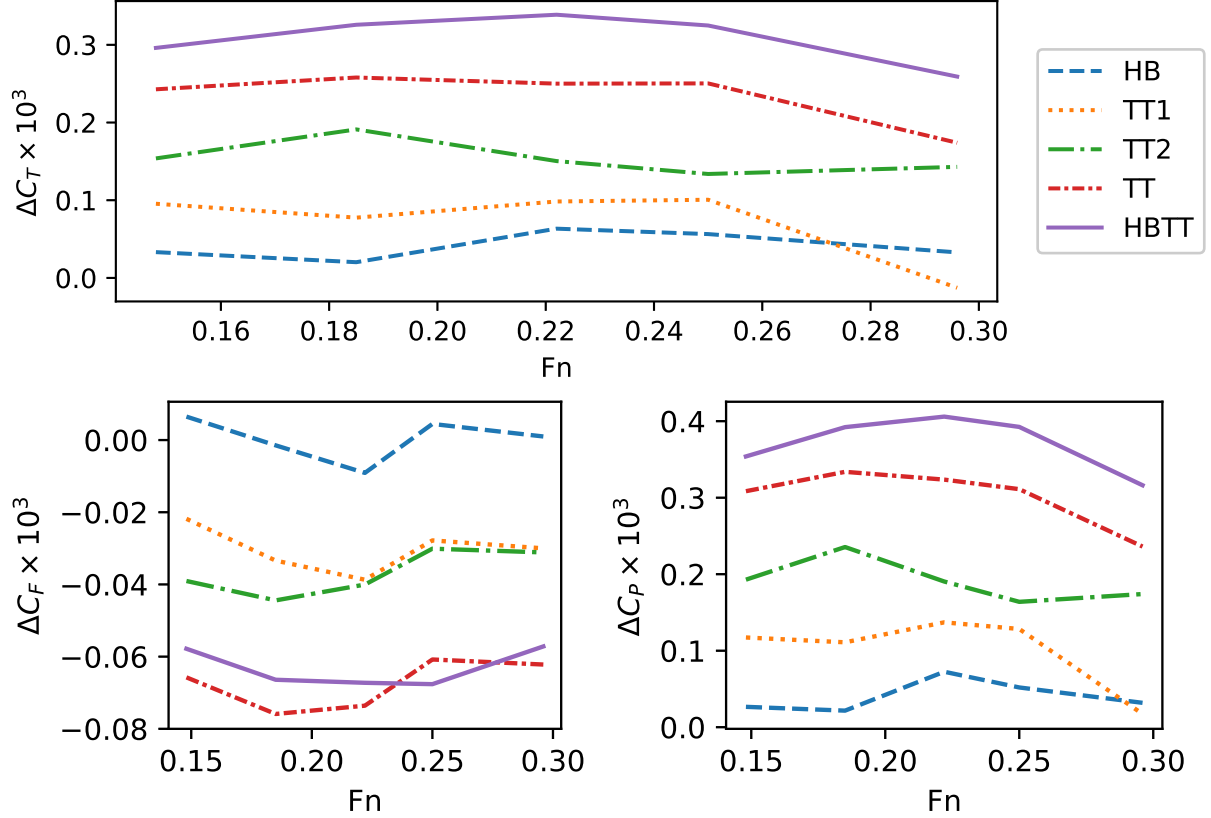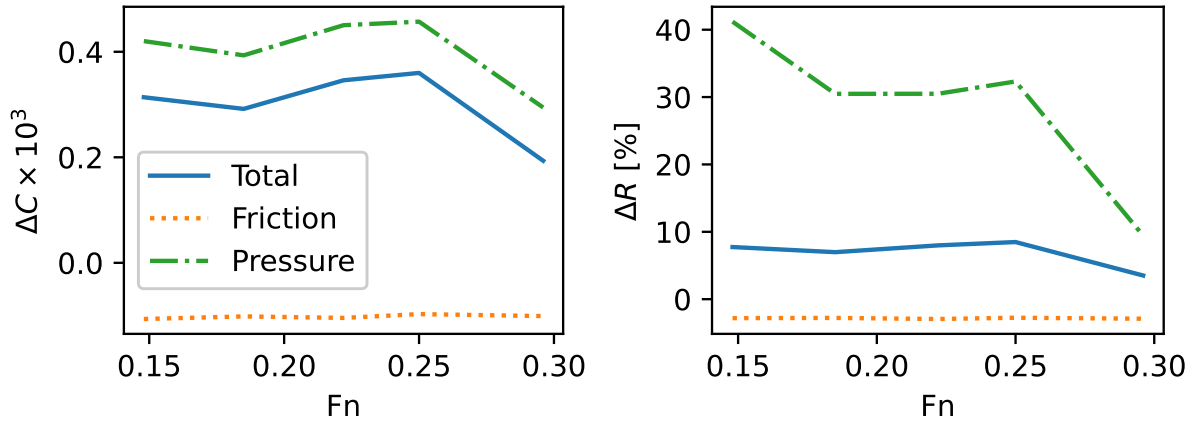
Figure 4.6: Changes in resistance coefficients from adding headbox (HB) and transverse bow tunnels. TT1 is only the foremost tunnel, TT2 only the second, and TT indicates that both tunnels are included.

1, and 0.0086 for tunnel 2. These results are plotted with the data points in Figure 4.8. The dotted black line is the Hollenbach estimate, while the stippled one corresponds to Stuntz.

The wake fraction for two considered cases is tabulated in Table 4.1. It is very sensitive to the measurement distance from the hull, but not longitudinal position. It has a mean value of 0.251 over all velocities with both bow tunnels fitted (TT), and 0.241 without them (naked). Least squares fitting Equation (2.15) to the data, using case specific wake factors and grid uncertainties, a form factor of 2.9 is found. The fit is plotted with the data points in Figure 4.9. Fitting is done with actual wake fractions, but the plot is made with a velocity mean between naked and TT to achieve one continuous curve.

To cross check fitted parameters, the analytical estimates for both tunnels and headboxes

Figure 4.7: Change in resistance from adding both headbox and transverse bow tunnels in model scale. Indicated both as percentage and change in resistance coefficiencts.
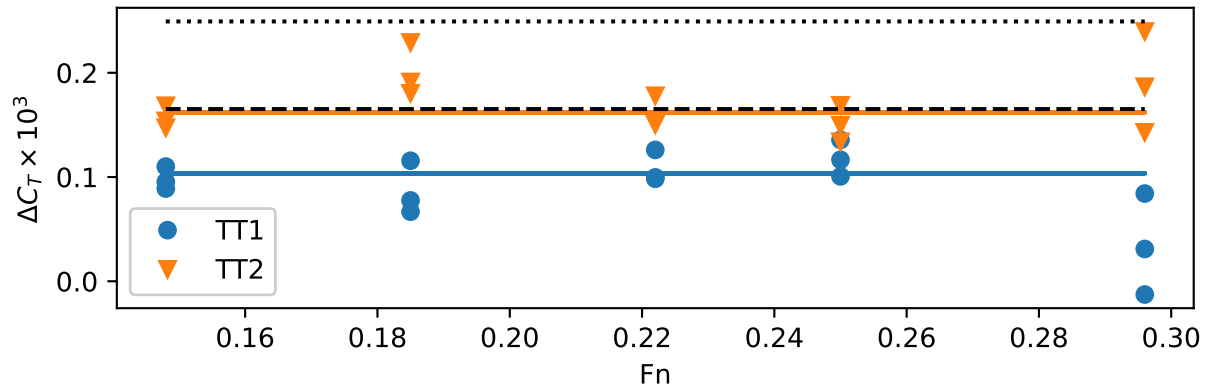
Figure 4.8: Comparisons of analytical estimates and meaured data for both bow tunnels. Full drawn lines are least squares fittings weighted with inverse discretization uncertainties. Dashed line is Stuntz's estimate for a single thruster, and stippled is Hollenbach's.

are added to the naked hull's resistance. This is shown to approximate the fully modified simulation's resistance with a mean error of 0.7%.

Fn	0.148	0.185	0.222	0.250	0.296	Mean
TT	0.232	0.235	0.249	0.262	0.275	0.251
Naked	0.227	0.231	0.246	0.236	0.266	0.241

Table 4.1: Wake fraction at headbox position for hull with and without bow tunnels
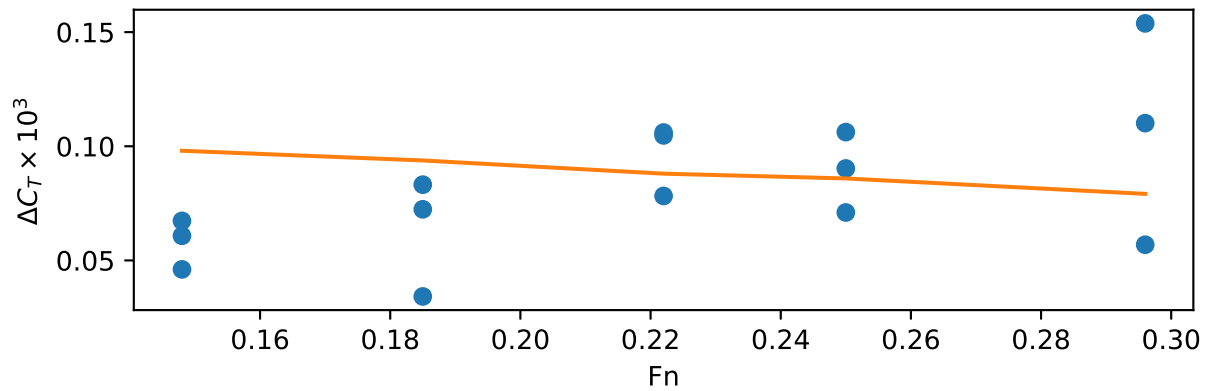
Figure 4.9: Least squares fittings and datapoints for headbox added resistance. The fit is weighted with inverse discretization uncertainties.

5 Discussion

5.1 Verification and validation

(a) h=3.7   **(b)** h=2.1   **(c)** h=1.1

Figure 5.1: Characteristic changes in the free surface development between mesh refinements
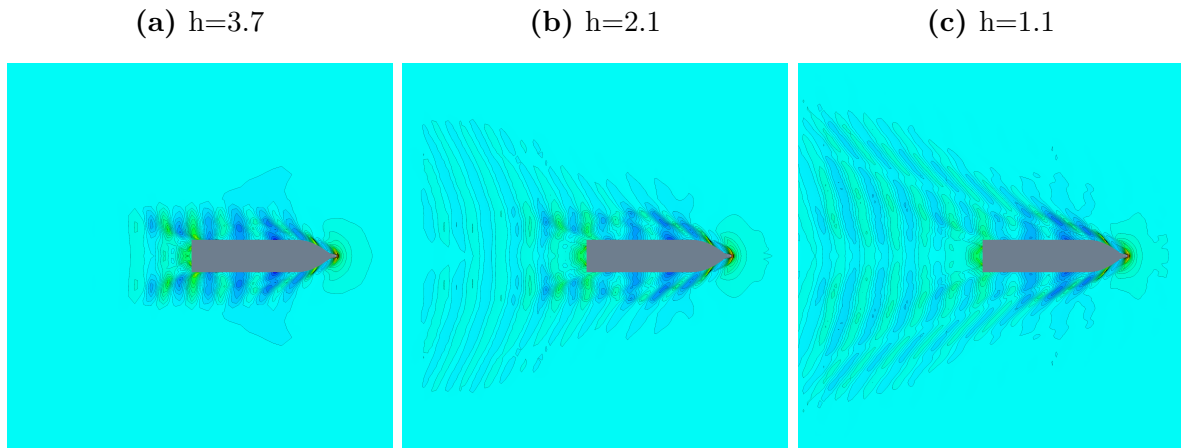
Results from the grid convergence studies are promising. Precise determination of total resistance is deemed most important, and this parameter generally shows good convergence. With near surface velocities determined by wall functions, the finer grids are likely most important for accurate wake resolution. Figure 5.1 shows how the wake at simulation end changes with mesh refinement.

Uncertainties of the model test results are not given. Towing tests done by researchers in the same towing tank suggests it is low[17, 16], with sum bias and precision errors being around 1% or lower for resistance, sinkage and trim. For resistance, this means that even with the smaller Grid-convergence index (GCI) uncertainties, there is overlap

between experimental and numerical confidence intervals in model scale. In addition, for the resistance, validation errors from GCI extrapolated results are much smaller than those for the the least squares method. However, the larger than 2 order of convergence for three of the velocities suggests underprediction of discretization uncertainties. For many of the remaining parameters, the calculated uncertainty is also either unreasonably low or high.

Full scale GCI uncertainty at Froude number 0.296 was found to be merely 0.6%, while deviation from scaled model test result is near 15%. This shows the risk of not having redundancy for the estimation of order of convergence when noise is present in the data. Excepting the two cases with near zero order of convergence for GCI, the least squares fitting approach gives consistently larger uncertainties. In all cases, its uncertainties appear more appropriate. A problem with adding the intermediate grids is that while they expose noise in the data, they may also introduce it. Between the three main grids, the refinement rate is around 1.9. After increasing to five grids, the ratio is barely above 1.3. This can make the apparent order of convergence less clear.

Least squares curve fitting has been applied for determination of numerical uncertainty for simulations of the test vessel KVLCC2 at Froude number 0.142[16]. The least squares approach is not identical to the one used here, but the computational setup largely is. For model scale total resistance, uncertainties of results are comparable. However, the KVLCC2 uncertainty estimates for sinkage and trim are significantly lower. For the current study, mean relative uncertainty for sinkage is 14.1%, but uncertainties are heavily skewed between velocities. At Froude number 0.296 it is only 1.1%, while it is 43.3% at 0.148. As mentioned in Section 2.1.3, it is speculated that poor CFD predictions of sinkage at low velocities is largely a precision problem. While the issues with numerical precision at lower velocities here are clear, accuracy does not improve with precision at higher velocities. This indicates a modeling error. As errors are largely consistent, it may stem from DFBI inputs, not necessarily from errors in the mathematical model. Static trim and sinkage has not been investigated. There is also the possibility of unaccounted for bias errors in the validation data. Variations in towing tank rails above water has

been pointed to as one such possibility[16].

In full scale, total resistance shows non-monotonic convergence for Froude number 0.296. The resistance is lowest at medium grids. With least squares fittings this is captured as a large uncertainty. It is speculated to stem from either the turbulence model, or the free surface model. k-ω SST is an isotropic turbulence model. Isotropy is directional independence, and here relates to rotational variance of the time-averaged turbulence quantities. The effect of assuming isotropy on resistance is uncertain, but when compared to the anisotropic EASM model, SST predicted aft segment resistance on KVLCC2 less accurately[16]. k-ω SST has also been shown to under predict the full scale ship wake, assumed caused by an inability to capture highly anisotropic turbulent flow[31].
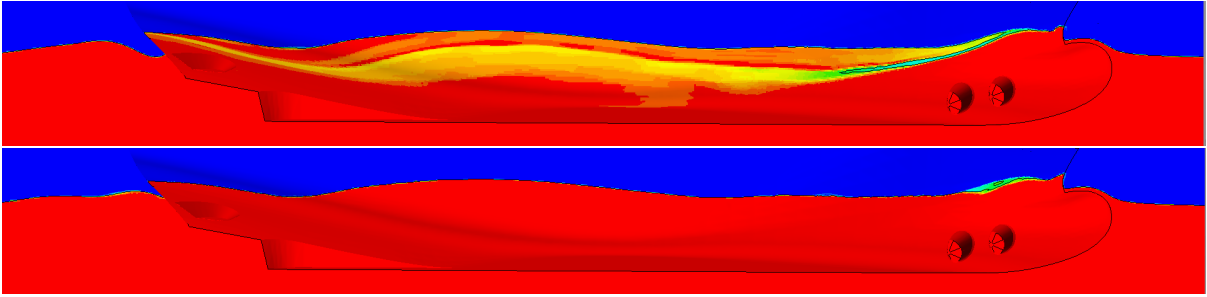
Figure 5.2: Volume fraction of fluid for the full scale vessel with and without suppression of numerical ventilation at Fn = 0.296

Another possible explanation of the poor high velocity results is issues with the volume of fluid (VOF) model. At Froude number 0.296, the total resistance coefficient increases dramatically. This is likely because it is above the effective range of the bulbous bow. The bow wave becomes larger, and splashing increases. As the mesh is refined, significant hull ventilation appears. This means that the volume of fluid model nonphysically predicts air to flow downwards along the hull. A ventilation suppression approach based on planing hulls is therefore implemented[1]. The basis of the approach is to simply replace any air phase below the water line with water once the simulation has reached equilibrium, and run for an additional time step with the new phase distribution. It is a highly pragmatic approach, obviously nonphysical from its breaking of continuity, but it is deemed sufficient for considering the fatality of the ventilation.

The suggested condition is to switch all cells in the domain with less than 50% air to 100% water. Due to the DFBI model, a single time step is not sufficient. The simulation must run until DFBI converges. To account for this extra duration, two additional conditions are added. They are that only cells below the waterline are considered, and that they must be no more than 5 centimeters from the hull surface. Figure 5.2 shows the volume ratio of water for the full scale hull at Froude number 0.296 with and without the adjustment. Total resistance is negligibly affected by the suppression scheme, with a change in the order of one tenth of a percent. Figure 5.2 shows that the stern wave is affected by the approach, but the influence of this on resistance is uncertain.

Ideally, full scale CFD should be validated against full scale experimental results. However, measuring full scale towing resistance is impractical, and the use of ITTC'78 scaled values for comparison has precedence in the literature[7]. Significant care should be taken when comparing to scaled results as their accuracy is not certain. Describing such comparisons as validation is inaccurate. Full scale ship resistance determined from towing tank experiments is affected by choice of extrapolation method. It has been shown that resistance results vary as much as 19% depending on method[29]. For model test based predictions, viscous forces can not be extrapolated. Instead, they are usually found by assuming constant form factors and using empirical regression parameters. Studies have shown that the form factor depends on both Froude and Reynolds number[29]. Viscous contributions to the resistance can not be completely separated from inviscid ones, so while a method may be accurate for typical hulls, it is not necessarily applicable for innovative hull forms. Accurate predictions require that the hull is comparable to the one empirical functions are developed for. Additionally, turbulence stimulators are used in model tests to achieve a full scale comparable flow regime, but the boundary layer is still relatively much thicker[7]. It is not yet fully understood how this aspect of flow physics transfers from model to full scale[15].

5.2 Added resistance

Added resistance results for the tunnels show generally good consistency. The tunnels appear relatively unaffected by each other, as seen from the small spreads in Figure 4.8. It is illustrated even clearer in Figure 5.3. The larger spread for Froude number 0.296 is consistent with the discretization uncertainty.
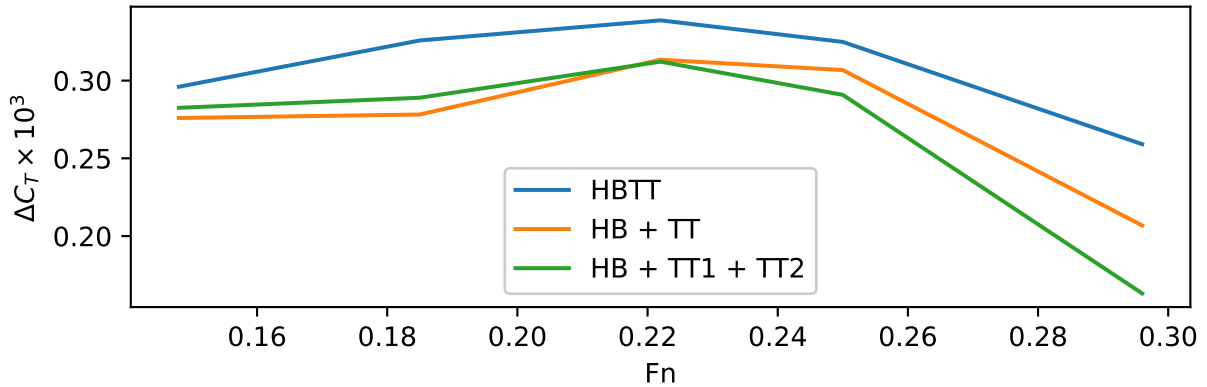
Figure 5.3: Sum added resistance from hull modifications by simulation and superposition.

The found tunnel drag coefficients correspond reasonably with empirical suggestions. Both are safely within Holtrop's range. Stuntz's estimate has near exact correspondence for tunnel 2, while Hollenbach's is overly conservative. The clear difference in added resistance from the two tunnels suggest that using a single value independently of tunnel placement is too simplistic. Holtrop's range of 0.003 to 0.012, depending on tunnel placement, appear to be the better solution. In this case, the longitudinal hull curvature is near identical between tunnel placements. However, tunnel 2 is placed lower on the hull, where the hull curves substantially towards the keel. The actual opening of tunnel 2 including edge chamfer is therefore 13% larger than for tunnel 1, despite equal tunnel diameter. This discrepancy may explain some of the difference in resistance coefficients.

Christensen's[9] estimate for the drag coefficient is not included in Figure 4.8, as it is assessed to be faulty. An alternate definition of Holtrop's formula for tunnel thruster

resistance is found in the literature[6]. It is presented in Equation (5.1).

$$R_{TH} = \rho \pi V^2 d_{TH} C_{D_{TH}}. \tag{5.1}$$

The difference from the one given in Equation (2.17) is that the tunnel diameter is not squared, and thus the equation is dimensionally erroneous. Christensen reports it this way. Insufficient data is provided for cross checking, but the low value of his suggested coefficient indicates that it in reality corresponds to $d_{TH} C_{D_{TH}} = 0.00174592$. Assuming this to be the case, tunnel diameters d_{TH} between 0.15 and 0.58 puts $C_{D_{TH}}$ within Holtrop's range. These are realistic dimensions for model scale transverse tunnels.

As seen in Figure 5.3, resistance results for the headboxes do not show the same consistency as for the tunnels. Their added resistance is considerably larger when they are fitted to a hull with tunnels than one without. This is counter intuitive. Table 4.1 shows that the wake fraction is higher for the hull with tunnels, meaning that velocity on the headboxes is lower. For Equation (2.15), the mean increase in wake fraction from adding tunnels corresponds to a 2.4% reduction in appendix resistance. From the data, the resistance is 69% higher instead. The added resistance of the headboxes is small, so for total hull resistance this difference is not overly significant. It may simply be a precision problem.

Another possibility is that the difference is caused by inaccuracies in applied mass or longitudinal center of gravity in the DFBI model. The mean trim over all velocities decreases by 9.8% when fitting headboxes to the naked hull, and 6.0% when fitting them to a tunneled one. Mean sinkage increases by 2.5% for the initially naked hull, and decreases by 0.4% for the initially tunneled one. To assess the significance of these changes, fixed trim and sinkage simulations are necessary.

The implicit Reynolds number dependence of Equation (2.15) can not be shown for the headboxes. With the correlation line in Equation (2.13), a larger Reynolds number means a smaller friction resistance coefficient, and thus a smaller total resistance coefficient with Equation (2.15). The contribution of the headboxes to the total resistance coefficient should then be decreasing with velocity. Figure 4.9 instead shows a constant,

or slightly increasing, contribution. For both tunnels and headboxes, added resistance is used for calculations, not forces acting on their actual surfaces. In the equations for tunnel resistance, this is assumed. In the equation for appendix resistance used for the headboxes, this is not the case. It is based on the assumption that appendix resistance is dominated by viscous effects, and that it does not affect the total pressure field. However, like for the tunnels, Figure 4.6 shows headbox contributions to be largely pressure dominated. This suggests that the changes the headboxes cause to the pressure field are more significant than their own drag. In the simulations, headbox friction resistance is increasing as expected by the square of the velocity, and it is largely unaffected by the fitting of tunnels. However, its magnitude is only 12 to 21 percent of the added resistance. The added resistance from headboxes should therefore be calculated similarly as from tunnels.

In model scale, the vessel is tested only with either both tunnels and headboxes or without any of them, so individual contributions may vary. However, the sum added resistance in model scale is comparable to full scale. Average $\Delta C_T \times 10^3$ is 0.30 in model scale, and 0.31 in full scale. There is a slight difference in distribution, with an average $\Delta C_F \times 10^3$ equal -0.10 in model scale, and -0.07 in full. The pressure resistance takes up the difference. This decrease in friction resistance is as expected, stemming from the increase in Reynolds number between scales. The pressure domination in both scales suggests that added resistance coefficients can be safely investigated in model scale.

Added resistance simulations are run with a coarser time step than fine grid solutions from grid convergence studies. Figure 4.3 shows results within 1% for the time steps, but time step independence of resistance can not be convincingly argued from it. In the end, time restraints motivated the use of a coarser time step.

6 Conclusion

The added resistance of transverse bow tunnels and headboxes is determined by full scale CFD simulations of a supply ship. Appropriate coefficients are found for use with analytical expressions for added resistance. Tunnels are shown to be largely unaffected by each other's presence, suggesting that their combined resistance contribution may be found by superposition. Headboxes appear to add more to the resistance when tunnels are already in place. Since this is improbable, it is deemed to simply expose inaccuracies of the CFD methodology.

Model scale simulations are shown to correspond well with towing tank results. In full scale, total resistance is overestimated compared to scaled model test values. However, CFD results appear to converge towards scaled values with increasing grid refinement. The limitations of scaled value comparisons are discussed.

Mean numerical uncertainty is larger in full scale than model scale, partly due to large uncertainties for the highest velocity. Possible explanations of these large uncertainties are discussed. The addition of tunnels and headboxes on the geometry do not add substantially to the uncertainty.

Total, non-dimensionalized added resistance in model scale is near identical to full scale values. The modifications are only considered separately in full scale, but the fact that their contributions are pressure dominated indicates that they may be accurately Froude scaled. With lower both numerical and modeling uncertainties, there is a clear argument for using model scale simulations for the prediction of added resistance from transverse tunnels and headboxes.

Bibliography

[1]   A.G. Avci and B. Barlas. "An experimental and numerical study of a high speed planing craft with full-scale validation". In: *Journal of Marine Science and Technology* 26 (2018), pp. 617–628.

[2]   C.B. Barrass and D.R. Derrett. "Chapter 40 - Rolling, pitching and heaving motions". In: *Ship Stability for Masters and Mates*. 6th ed. Elsevier Ltd, 2006, pp. 356–365.

[3]   V. Bertram and J. Marzi. "On The Economical Importance Of Interfacing CAD And CFD". In: *Transactions on the Built Environment* 1 (1993).

[4]   J.L. Beveridge. *Design and Performance of Bow Thrusters*. Tech. rep. 1971.

[5]   L. Birk. *Fundamentals of ship hydrodynamics : fluid mechanics, ship resistance and propulsion*. John Wiley & Sons Ltd, 2019, pp. 616, 637–638. ISBN: 9781118855485.

[6]   J.S. Carlton. *Marine propellers and propulsion*. 2nd ed. Elsevier Butterworth-Heinemann, 2007, p. 303. ISBN: 1-281-01932-1.

[7]   A.M. Castro, P.M. Carrica, and F. Stern. "Full scale self-propulsion computations using discretized propeller for the KRISO container ship KCS". In: *Computers and Fluids* 51 (2011), pp. 35–47.

[8]   I. B. Celik et al. "Procedure for Estimation and Reporting of Uncertainty Due to Discretization in CFD Applications". In: *Journal of Fluids Engineering* 130 (2008). 078001.

[9]   V. Christensen. "Numerical calculation of ship appendage resistance using CFD". MA thesis. Norwegian university of science and technology, 2019.

[10] P. Crepier. "Ship resistance prediction: Verification and validation exercise on unstructured grids". In: *VII International Conference on Computational Methods in*

Marine Engineering (Marine 2017). Ed. by M. Visonneau, P. Queutey, and D. Le Touzé. International Center for Numerical Methods in Engineering, 2017, pp. 365–376.

[11] S. Dong et al. "CFD-based Hull Form Resistance and Flow Field Multi-objective Optimization Research". In: *The proceedings of the Twenty-fourth (2014) International Ocean and Polar Engineering Conference*. International Society of Offshore and Polar Engineers, 2014, pp. 714–720.

[12] L. Eca and M. Hoekstra. "A procedure for the estimation of the numerical uncertainty of CFD calculations based on grid refinement studies". In: *Journal of Computational Physics* 262 (2014), pp. 104–130.

[13] J.H. Ferziger, M. Perić, and R.L. Street. *Computational Methods for Fluid Dynamics*. 4th ed. Springer International Publishing, 2020. ISBN: 9783319996912.

[14] B. Godderidge et al. "The simulation of free surface flows with Computational Fluid Dynamics". In: *2008 Ansys UK User Conference: Inspiring Engineering*. Ansys, 2008.

[15] J.J. Gorski. "Present state of numerical ship hydrodynamics and validation experiments". In: *Proceedings of the 20th international conference on offshore mechanics and arctic engineering*. American Society of Mechanical Engineers, 2001.

[16] B.J. Guo, G.B. Deng, and S. Steen. "Verification and validation of numerical calculation of ship resistance and flow field of a large tanker". In: *Ships and Offshore Structures* 8 (2013), pp. 3–14.

[17] J.B. Ildstad. "Use of Turbulence Stimulation on Ship Models". MA thesis. Norwegian University of Science and Technology, 2018.

[18] International Towing Tank Conference (ITTC). *1978 ITTC performance prediction method*. 4th ed. ITTC - Recommended procedures and guidelines. 2017.

[19] International Towing Tank Conference (ITTC). *Practical guidelines for ship CFD applications*. 1st ed. ITTC - Recommended procedures and guidelines. 2014.

[20] H. Jasak et al. "CFD validation and grid sensitivity studies of full scale ship self propulsion". In: *International Journal of Naval Architecture and Ocean Engineering* 11 (2019), pp. 33–43.

[21]   I.M. Kamal, M.S. Rasahidan, and Y.A. Ahmed. "Scaling of RV Athena's Appendage Drag using CFD". In: *Advancement in Emerging Technologies and Engineering Applications*. Ed. by C.L. Saw et al. Lecture Notes in Mechanical Engineering. Springer Singapore, 2020, pp. 79–89.

[22]   G.-H. Kim and S. Park. "Development of a numerical simulation tool for efficient and robust prediction of ship resistance". In: *International Journal of Naval Architecture and Ocean Engineering* 9 (2017), pp. 537–551.

[23]   L. Larsson, F. Stern, and M. Visonneau. "CFD in Ship Hydrodynamics: Results of the Gothenburg 2010 Workshop". In: *MARINE 2011, IV International Conference on Computational Methods in Marine Engineering*. Vol. 29. Springer Dordrecht, 2014, pp. 237–259.

[24]   F.R. Menter. "Two-equation eddy-viscosity turbulence models for engineering applications". In: *AIAA Journal* 32 (1994), pp. 1598–1605.

[25]   F.R. Menter, M. Kuntz, and R. Langtry. "Ten years of industrial experience with the SST turbulence model". In: *Turbulence, Heat and Mass Transfer*. Ed. by K. Hanjalić, Y. Nagano, and M.J. Tummers. Vol. 4. Begell House.

[26]   A.F. Molland, S.R Turnock, and D.A. Hudson. *Ship Resistance and Propulsion*. Cambridge University Press, 2011. ISBN: 9780521760522.

[27]   I. Morenko and V. Fedyaev. "Influence of turbulence intensity and turbulence length scale on the drag, lift and heat transfer of a circular cylinder". In: *China Ocean Engineering* 31 (2017), pp. 357–363.

[28]   S. Muzaferija and M. Peric. "Computation of free-surface flows using interface-tracking and interface-capturing methods". In: *Nonlinear water wave interaction*. Ed. by O. Mahrenholtz and M. Markiewicz. Vol. 24. Advances in fluid mechanics. WIT Press, 1999. ISBN: 1853125458.

[29]   K. Niklas and H. Pruszko. "Full-scale CFD simulations for the determination of ship resistance as a rational, alternative method to towing tank experiments". In: *Ocean Engineering* 190 (2019).

[30] D.W. Park and S.B. Lee. "The sensitivity of ship resistance to wall-adjacent grids and near-wall treatments". In: *International Journal of Naval Architecture and Ocean Engineering* 10 (2018), pp. 683–691.

[31] D. Ponkratov and C. Zegos. "Validation of Ship Scale CFD Self-Propulsion Simulation by the Direct Comparison with Sea Trials Results". In: *Proceedings of the Fourth International Symposium on Marine Propulsors (SMP'15)*. SMP Chair Committee, 2015.

[32] P.J. Roache. "Perspective: A method for uniform reporting of grid refinement studies". In: *Journal of Fluids Engineering* 116 (1994), pp. 405–413.

[33] P.J. Roache. "Quantification of uncertainty in computational fluid dynamics". In: *Annual Review of Fluid Mechanics* 29 (1997), pp. 123–160.

[34] F.G. Schmitt. "About Boussinesq's turbulent viscosity hypothesis: historical remarks and a direct evaluation of its validity". In: *Comptes Rendus Mécanique* 335 (2007), pp. 617–627.

[35] H. Schneekluth. *Ship design for efficiency and economy*. 2nd ed. Butterworth-Heinemann, 1998. ISBN: 0750641339.

[36] Siemens. *Simcenter Star-ccm+ documentation*. Accessed 15.01.2020 - 10.06.2020. Requires login. 2020. URL: https://thesteveportal.plm.automation.siemens.com/.

[37] R. Sims et al. "Working Group III Contribution to the Fifth Assessment Report of the Intergovernmental Panel on Climate Change". In: *Climate Change 2014: Mitigation of climate change*. Cambridge University Press, 2014. Chap. 8.

[38] S. Spence. "Numerical Investigation of Free Surface Flows". MA thesis. Norwegian University of Science and Technology, 2014.

[39] Sverre Steen. *Kompendium - motstand og propulsjon*. Institutt for marin teknikk - NTNU Trondheim, 2011.

[40] Q. Zeng et al. "A modification of the ITTC'57 correlation line for shallow water". In: *Journal of Marine Science and Technology* 24 (2019), pp. 642–657.

[41] Y.A. Çengel and J.M Cimbala. *Fluid mechanics : fundamentals and applications*. 3rd edition in SI units. McGraw-Hill, 2014, pp. 573–575,904–905. ISBN: 9781259011221.

A   Appendix

A.1   Grid convergence of resistance for naked full scale vessel
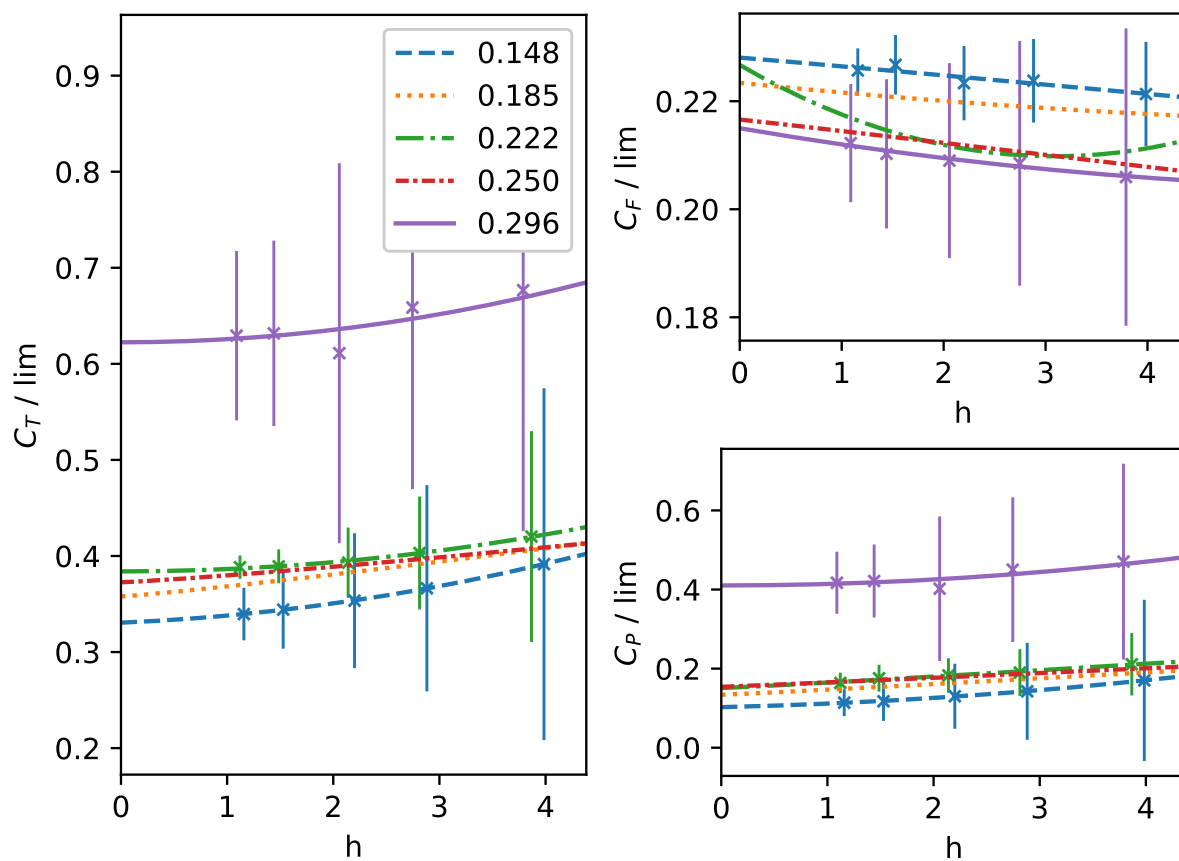
Figure A.1: Mesh convergence of resistance for full scale vessel without headbox and transverse tunnels. Line labels state the Froude number.

A.2 Grid convergence of ship motions

(a) Full scale with headbox and transverse tunnels
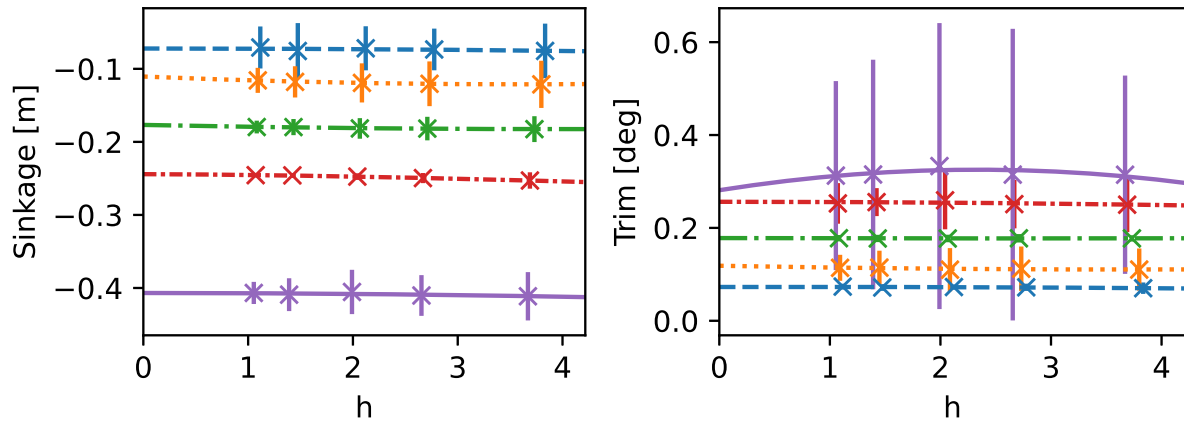
(b) Full scale without headbox and transverse tunnels
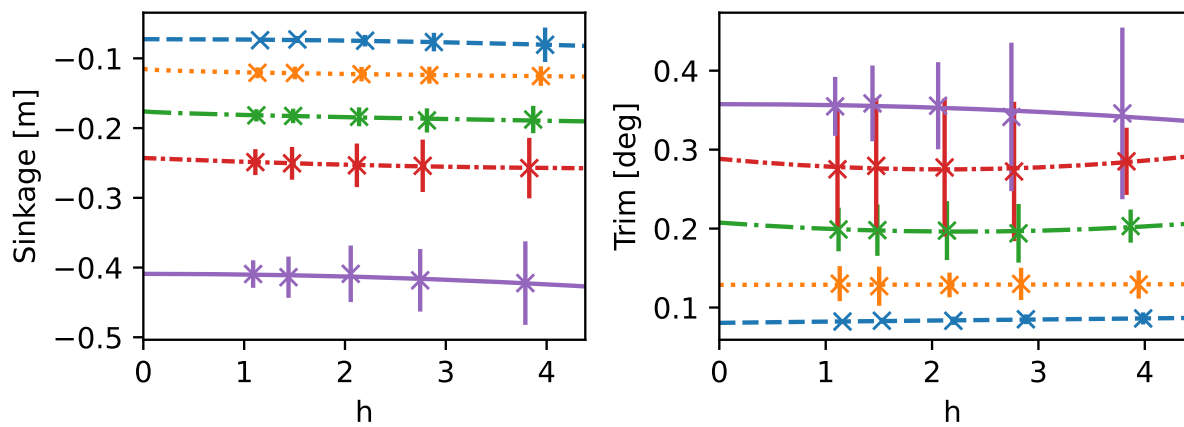
(c) Model scale with headbox and transverse tunnels

Figure A.2: Mesh convergence of ship motions. Line labels are given in Figure A.1.

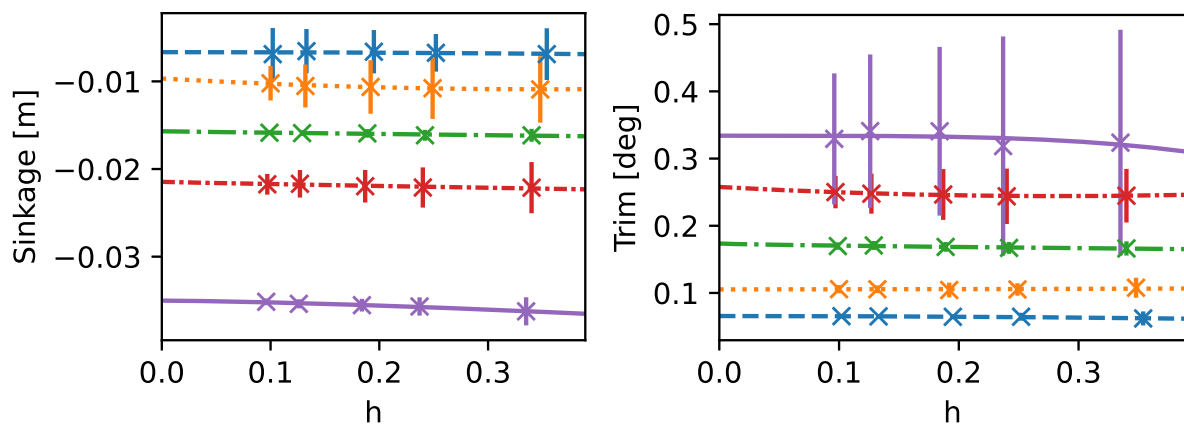## A.3   Grid convergence tables

Fn [-]	0.148	0.185	0.222	0.250	0.296	0.148	0.185	0.222	0.250	0.296
	Model scale with tunnels and headboxes									
R_T	1.9	1.8	2.9	7.4	2.4	1.4	1.1	2.0	M	M
R_F	0.0	1.1	0.3	2.7	0.6	0.9	2.0	0.6	M	1.0
R_P	1.5	1.6	1.6	3.0	2.0	1.3	1.4	1.4	M	M
Sinkage	0.0	0.5	1.9	0.3	1.1	2.0	M	0.9	0.9	1.5
Trim	1.8	1.7	1.2	0.9	0.7	2.0	2.0	0.7	M	3.8
	Full scale with tunnels and headboxes									
R_T	1.2	1.6	1.1	1.3	2.8	1.2	1.5	1.0	1.6	2.0
R_F	0.0	0.5	0.6	1.0	1.3	M	M	0.9	M	1.1
R_P	1.0	1.3	1.0	1.0	3.2	1.0	1.2	1.0	1.0	2.0
Sinkage	2.0	0.7	0.9	1.8	2.4	2.0	M	M	1.6	2.0
Trim	1.7	4.1	1.6	0.6	0.2	M	M	M	2.0	M
	Full scale without tunnels and headboxes									
R_T	1.8	1.4	3.0	0.9	2.1	1.7	1.1	2.0	1.2	2.0
R_F	0.1	0.6	2.4	0.4	0.0	1.0	M	M	1.0	M
R_P	1.6	1.1	0.8	0.8	2.5	1.7	1.1	1.1	1.0	2.0
Sinkage	3.7	0.6	1.2	0.1	6.0	2.0	0.5	0.7	M	2.0
Trim	2.0	1.6	2.3	2.1	4.1	0.9	2.0	M	M	2.0

Table A.1: Apparent order of convergence for all parameters. GCI on the left, least squares fitting on the right. M signifies mixed first and second order convergence.

Fn [-]	0.148	0.185	0.222	0.250	0.296	0.148	0.185	0.222	0.250	0.296
Model scale with tunnels and headboxes										
R_T	0.9	1.1	0.2	0.0	0.6	2.8	4.2	2.0	3.1	7.5
R_F	74.4	1.4	14.1	0.5	4.6	1.8	1.4	4.5	9.5	5.2
R_P	6.4	4.9	3.4	0.5	2.3	9.4	7.4	5.6	14.3	17.6
Sinkage	325.9	15.0	0.2	5.6	1.4	43.3	19.2	1.7	5.4	1.1
Trim	0.8	0.7	0.8	2.4	7.9	1.9	5.8	3.2	9.6	29.6
Full scale with tunnels and headboxes										
R_T	6.2	2.3	4.2	3.6	0.6	7.7	5.1	6.3	3.0	13.9
R_F	101.3	8.2	7.0	4.2	1.4	11.3	10.6	3.7	13.4	2.2
R_P	22.5	9.6	12.8	15.6	0.4	26.8	15.5	14.2	15.5	8.0
Sinkage	0.7	6.2	1.8	0.5	0.1	40.6	14.8	4.9	0.8	3.7
Trim	0.8	0.3	0.2	7.7	79.7	8.4	24.5	3.9	17.3	65.1
Full scale without tunnels and headboxes										
R_T	2.4	2.4	0.2	3.7	1.3	2.7	6.1	3.1	4.1	14.0
R_F	16.8	3.3	1.0	5.8	96.6	1.8	5.8	19.8	1.9	5.2
R_P	10.0	10.9	20.9	13.5	1.2	10.3	16.1	15.8	12.0	18.8
Sinkage	0.1	4.1	1.3	46.4	0.0	5.0	6.4	4.8	7.5	4.8
Trim	0.5	0.9	0.3	0.4	0.0	3.5	17.0	13.9	27.8	10.5

Table A.2: Relative grid convergence uncertainties in percent for all parameters. GCI on the left, least squares fitting on the right.

A.4 Percentage added resistance in full scale
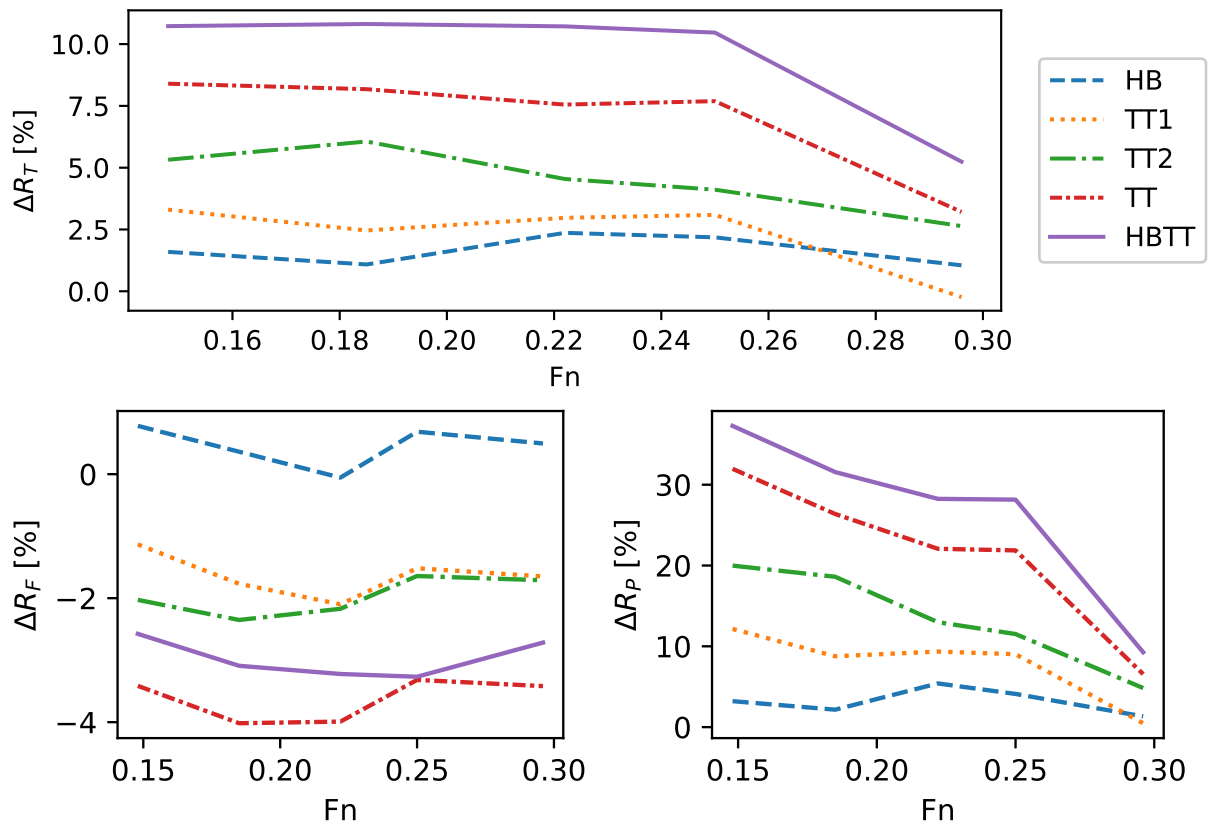
Figure A.3: Percentage change in resistance from adding headbox (HB) and transverse bow tunnels. TT1 is only the foremost tunnel, TT2 only the second, and TT indicates that both tunnels are included.